

# The NewHorizon Simulation - To Bar Or Not To Bar

J. Reddish<sup>1</sup>★, K. Kraljic<sup>1,2</sup>†, M. S. Petersen<sup>1,3</sup>, K. Tep<sup>1,3</sup>, Y. Dubois<sup>3</sup>, C. Pichon<sup>1,3,4</sup>,  
S. Peirani<sup>5,3</sup>, F. Bournaud<sup>6,7</sup>, H. Choi<sup>8</sup>, J. Devriendt<sup>9</sup>, R. Jackson<sup>8</sup>, G. Martin<sup>11,12</sup>,  
M. J. Park<sup>13</sup>, M. Volonteri<sup>3</sup>, S. K. Yi<sup>8</sup>

<sup>1</sup> Institute for Astronomy, University of Edinburgh, Royal Observatory, Edinburgh, EH9 3HJ, UK

<sup>2</sup> Aix Marseille Université, CNRS, CNES, UMR 7326, Laboratoire d'Astrophysique de Marseille, Marseille, France

<sup>3</sup> Institut d'Astrophysique de Paris, UMR 7095, CNRS, UPMC Univ. Paris VI, 98 bis boulevard Arago, 75014 Paris, France

<sup>4</sup> Korea Institute of Advanced Studies (KIAS) 85 Hoegiro, Dongdaemun-gu, Seoul, 02455, Republic of Korea

<sup>5</sup> Université Côte d'Azur, Observatoire de la Côte d'Azur, CNRS, Laboratoire Lagrange, Nice, France

<sup>6</sup> AIM, CEA, CNRS, Université Paris-Saclay, Université Paris Diderot, Sorbonne Paris Cité, 91191 Gif-sur-Yvette, France

<sup>7</sup> IRFU, CEA, Université Paris-Saclay, 91191 Gif-sur-Yvette, France

<sup>8</sup> Department of Astronomy and Yonsei University Observatory, Yonsei University, Seoul 03722, Republic of Korea

<sup>9</sup> Department of Physics, University of Oxford, Keble Road, Oxford OX1 3RH, United Kingdom

<sup>11</sup> Korea Astronomy and Space Science Institute, 776 Daedeokdae-ro, Yuseong-gu, Daejeon 34055, Republic of Korea

<sup>12</sup> Steward Observatory, University of Arizona, 933 N. Cherry Ave, Tucson, AZ 85719, USA

<sup>13</sup> Center for Astrophysics | Harvard & Smithsonian, 60 Garden St., Cambridge, MA 02138, USA

Accepted XXX. Received YYY; in original form ZZZ

## ABSTRACT

We use the NEWHORIZON simulation to study the redshift evolution of bar properties and fractions within galaxies in the stellar masses range  $M_{\star} = 10^{7.25} - 10^{11.4} M_{\odot}$  over the redshift range  $z = 0.25 - 1.3$ . We select disc galaxies using stellar kinematics as a proxy for galaxy morphology. We employ two different automated bar detection methods, coupled with visual inspection, resulting in observable bar fractions of  $f_{\text{bar}} = 0.070^{+0.018}_{-0.012}$  at  $z \sim 1.3$ , decreasing to  $f_{\text{bar}} = 0.011^{+0.014}_{-0.003}$  at  $z \sim 0.25$ . Only one galaxy is visually confirmed as strongly barred in our sample. This bar is hosted by the most massive disk and only survives from  $z = 1.3$  down to  $z = 0.7$ . Such a low bar fraction, in particular amongst Milky Way-like progenitors, highlights a missing bars problem, shared by literally all cosmological simulations with spatial resolution  $< 100$  pc to date. The analysis of linear growth rates, rotation curves and derived summary statistics of the stellar, gas and dark matter components suggest that galaxies with stellar masses below  $10^{9.5} - 10^{10} M_{\odot}$  in NEWHORIZON appear to be too dominated by dark matter relative to stellar content to form a bar, while more massive galaxies typically have formed large bulges that prevent bar persistence at low redshift. This investigation confirms that the evolution of the bar fraction puts stringent constraints on the assembly history of baryons and dark matter onto galaxies.

**Key words:** galaxies: bar – galaxies: evolution – galaxies: disc – galaxies: bulges – methods: data analysis

## 1 INTRODUCTION

Stellar bars are not only visually striking, they also play an important role in the evolution of disc galaxies, allowing them to redistribute their angular momentum (Lynden-Bell & Kalnajs 1972; Lynden-Bell 1979; Tremaine & Weinberg 1984; Weinberg 1985; Athanassoula & Sellwood 1986). Bars are commonly thought to form spontaneously in stellar discs that are sufficiently massive and dynamically cold to be gravitationally unstable (e.g. Toomre 1963;

Combes & Sanders 1981; Athanassoula & Sellwood 1986; Combes & Elmegreen 1993). Once formed, simulations show that bars can evolve through angular momentum exchange with both the dark matter haloes (e.g. Debattista & Sellwood 2000), and with the stellar and gaseous discs (Bournaud & Combes 2002; Bournaud et al. 2005). Bars may be amplified through the transfer of angular momentum to the dark matter halo (e.g. Athanassoula 2008; Kormendy 2013; Petersen et al. 2016, 2019b). However, they can also be weakened or destroyed if they gain too much angular momentum from infalling gas (Bournaud et al. 2005) or from excessive growth of the central mass concentration of a galaxy – specifically, simulations suggest that short bars of  $\sim 1$  kpc may be destroyed by the growth

★ E-mail: reddishjames7@gmail.com

† E-mail: katarina.kraljic@lam.fr

of a galaxies central concentration (e.g. Hasan & Norman 1990; Hasan et al. 1993; Shen & Sellwood 2004) henceforth impacting significantly on the growth of a central bulge without the involvement of a galaxy merger (e.g. Du et al. 2017; Guo et al. 2020). With these statements, it is important to highlight the caveat made by many of these referenced works whereby these scenarios are not yet supported by observational evidence (see Shen & Sellwood 2004; Athanassoula et al. 2005, and references therein for further discussions).

Simulations have shown that bars may also be affected by the conditions of their host galaxy. They may be reinforced or reformed given sufficient accretion of external gas onto the disc (Bournaud & Combes 2002) as well as also being destroyed or (re-)formed as a result of environmental factors such as tidal interactions or galaxy mergers (e.g. Hohl 1971; Noguchi 1987; Gerin et al. 1990; Berentzen et al. 2004; Peirani et al. 2009; Moetazedian et al. 2017; Cavanagh & Bekki 2020; Zhou et al. 2020). In its host galaxy, the presence of a bar might also effect the formation of a pseudo-bulge at the galaxy’s centre (e.g. Pfenniger & Norman 1990; Kormendy & Kennicutt 2004; Athanassoula 2012; Kormendy 2013; Lin et al. 2020). However, we note that for these scenarios, observational evidence is as yet unclear. Several observational studies (e.g. Sérsic & Pastoriza 1965; Martinet & Friedli 1997; Sheth et al. 2005; Ellison et al. 2011; Lin et al. 2020) suggest that bars might enhance the star formation at the centre of the galaxy, but may also play a role in the cessation of star formation (e.g. Masters et al. 2012; Wang et al. 2012; Fraser-McKelvie et al. 2020). Inflowing gas driven by a bar has also long been implicated in the fuelling of the central active galactic nuclei (AGN) (e.g. Knapen et al. 2000; Oh et al. 2012; Galloway et al. 2015; Alonso et al. 2018), although again, compelling observational evidence is still missing (e.g. Regan & Mulchaey 1997; Cisternas et al. 2013; Cheung et al. 2015; Cisternas et al. 2015; Oh et al. 2012). It therefore seems apparent that bars play a key role in the evolution of disc galaxies (see Kormendy & Kennicutt 2004; Kormendy 2013, however, for an opposing view, see van den Bergh 2011, and references therein).

In spite of the existence of increasingly constrained observational measurements of the frequency of bars in the local Universe (e.g. Eskridge et al. 2000; Whyte et al. 2002; Laurikainen et al. 2004; Menéndez-Delmestre et al. 2007; Marinova & Jogee 2007; Barazza et al. 2008; Aguerri et al. 2009; Sheth et al. 2008; Masters et al. 2011, 2012; Oh et al. 2012; Melvin et al. 2014; Díaz-García et al. 2016), and a number of galaxy simulations routinely forming bars (e.g. Ostriker & Peebles 1973; Hohl 1976; Athanassoula 2008, 2012; Algorry et al. 2017; Zhou et al. 2020; Rosas-Guevara et al. 2020, 2021), their origin and details on their life-cycle are still not fully understood. Studying the frequency of bars and the evolution through redshift as a function of stellar mass provides an opportunity to learn about the formation and persistence of bars.

In the local Universe, the fraction of barred galaxies is quite well established. Both optical and near infrared observations reveal that roughly 2/3 (or 1/3 if only so-called “strong” bars are counted) of nearby spiral galaxies host a bar (e.g. Eskridge et al. 2000; Whyte et al. 2002; Laurikainen et al. 2004; Menéndez-Delmestre et al. 2007; Barazza et al. 2008; Sheth et al. 2008; Aguerri et al. 2009; Nair & Abraham 2010; Masters et al. 2011, 2012; Melvin et al. 2014; Díaz-García et al. 2016). However, depending on the bar classification method, the strength of the bars observed, which wavebands they have been observed in and the process of disc galaxy selection, this value can vary. By analysing the sample of spiral galaxies in the Spitzer Survey of Stellar Structure in Galaxies (S<sup>4</sup>G) in the nearby Universe ( $z < 0.01$ ), Erwin (2018) found that the

fraction of barred galaxies,  $f_{\text{bar}}$ , reaches a maximum of  $\sim 70\%$  at galaxy stellar mass  $\sim 10^{9.7} M_{\odot}$  and then declines for both higher and lower masses. These measurements are in a good agreement with previous S<sup>4</sup>G based study of Díaz-García et al. (2016) once the same galaxy selection is applied (see Erwin 2018, for a more detailed discussion). Such findings are however in contrast to most Sloan Digital Sky Survey (SDSS) based studies (e.g. Masters et al. 2012; Oh et al. 2012; Melvin et al. 2014) which report a strongly increasing  $f_{\text{bar}}$  with stellar mass (for  $M_{\odot} > 10^{10} M_{\odot}$  typically). As suggested by Erwin (2018) - and demonstrated via a simulated cut in bar size - this discrepancy may be the consequence of the significant challenge that SDSS-based studies have in picking out smaller bars in galaxies with stellar mass  $< 10^{10} M_{\odot}$ ; the ensuing underestimate of the bar fraction at these stellar masses results in the incapability of tracing a peak in bar fraction at  $\sim 10^{9.7} M_{\odot}$ .

The bar fraction is less well constrained out to high redshifts due to a lack of spatial resolution necessary to resolve bars. Early conflicting results on whether the bar fraction declines towards higher redshifts (e.g. Abraham et al. 1999) or stays roughly constant up to  $z \sim 1$  (e.g. Jogee et al. 2004; Elmegreen et al. 2004; Sheth et al. 2003) are today interpreted as being due to the selection bias in shallow or low resolution data targeting more massive or large systems (Sheth et al. 2008). Thanks to the high resolution deep optical and near-infrared data, it is today established that the fraction of barred galaxies decreases with increasing redshift (e.g. Cameron et al. 2010; Melvin et al. 2014; Simmons et al. 2014). These high redshift studies focus primarily on stellar masses above  $10^{10} M_{\odot}$  finding increasing bar fractions with stellar masses at all redshifts up to  $z \sim 1$  (e.g. Melvin et al. 2014).

Numerical simulations provide a powerful tool in studying the formation and evolution of bars. Large-scale hydrodynamical simulations, e.g. ILLUSTRIS (Vogelsberger et al. 2014), ILLUSTRIS TNG (Pillepich et al. 2018), EAGLE (Schaye et al. 2015) or HORIZON-AGN (Dubois et al. 2016), all reproduce a morphological mix of galaxies that is in a good agreement with the well established observational results. These simulations have a typical spatial resolution of  $\sim 1$  kpc which is insufficient for properly resolving the scale height of galactic discs and therefore for studying bars. However, some recent studies attempted to quantify properties of barred galaxies in a cosmological hydrodynamical realisations of the IllustrisTNG suite - the TNG100 simulation (Rosas-Guevara et al. 2020; Zhou et al. 2020; Zhao et al. 2020) and the TNG50 simulation (Rosas-Guevara et al. 2021) - in ILLUSTRIS (Peschken & Lokas 2019) and in EAGLE (Algorry et al. 2017). They principally focused on disc galaxies with stellar masses  $M_{\star} \geq 10^{10-10.5} M_{\odot}$  mostly at  $z = 0$ , but some extended the analysis to higher redshifts (Peschken & Lokas 2019; Zhao et al. 2020; Rosas-Guevara et al. 2021). Overall, while at  $z = 0$  these cosmological simulations produce a fraction of barred galaxies from about 20% (in ILLUSTRIS; Peschken & Lokas 2019) and 30% (in TNG50; Rosas-Guevara et al. 2021) to about 40%-60% (in EAGLE; Algorry et al. 2017, and in TNG100; Rosas-Guevara et al. 2020; Zhao et al. 2020), they generally overproduce bars at  $z = 0$  at high masses ( $M_{\star} \geq 10^{10.5} M_{\odot}$ ) and tend to suppress their formation at low masses (in the stellar mass range  $M_{\star} \sim 10^{10-10.5} M_{\odot}$ ) compared to observations (Erwin 2018). These simulations also fail to reproduce the declining bar fraction with increasing redshift, seen in most observations.

Idealised simulations reach high enough resolutions to study bars in great detail (e.g. Debattista & Sellwood 2000; Athanassoula 2002; Berentzen et al. 2004; Athanassoula 2012), however, in order to study the cosmic evolution of bar fraction, galaxies need to be modelled self-consistently, within the cosmological context, and

with sufficiently high resolution, e.g. by using zoom-in simulations (e.g. Kraljic et al. 2012; Scannapieco & Athanassoula 2012; Zana et al. 2018, 2019; Blázquez-Calero et al. 2020). Sufficient resolution in recent cosmological simulations have allowed study into the evolution of detailed structure in disk galaxies (e.g. Guedes et al. 2011; Stinson et al. 2013; Marinacci et al. 2014; Okamoto et al. 2015). However, obtaining a statistically significant sample of galaxies for a meaningful study of bar fractions remains difficult. One notable exception is the work of Kraljic et al. (2012) analysing a sample of cosmological zoom-in simulations of 33 Milky Way-mass galaxies. They found that the fraction of observable bars among spiral galaxies drops from about 80% at  $z = 0$  to about 15% at  $z \sim 1$  and to almost zero at  $z \sim 2$ . The emergence of bars in the studied mass range was established to redshift  $z \sim 0.8 - 1$ .

In this paper we present a study of the bars in the recent high-resolution cosmological simulation NEWHORIZON (Dubois et al. 2021), modelling the population of galaxies with low-to-intermediate stellar masses ( $10^{7.25}M_{\odot} \lesssim M_{\star} \lesssim 10^{11.4}M_{\odot}$ ) in an average density region probing field and group environments. This mass range is wider than previously studied in simulations (e.g. Athanassoula 2008, 2012; Rosas-Guevara et al. 2020; Zhou et al. 2020), which typically focus on Milky Way-mass galaxies ( $M_{\star} \sim 10^{10-11}M_{\odot}$ ). We analyse the structure of a large sample of galaxies extracted from the simulation from redshift  $z = 1.3$  down to redshift  $z = 0.25$  in order to constrain the evolution of the bar fraction over this redshift range. Studying galaxies across both mass and time is crucial for accurately characterising the presence (or lack) of bars. Similar exercise for future observational data will also help create a more accurate census for bar fraction, in particular toward lower masses and higher redshifts.

This work is a comprehensive look at the bar fraction across a wide range in stellar mass and across a significant fraction of cosmic time. We implement two different automated bar detection methods so as to provide a more robust measurement of the fraction of barred galaxies. These results are then discussed on an object-by-object basis and as populations, using two distinct summary statistics. The paper is organised as follows. In Section 2, we present a description of the NEWHORIZON simulation along with the process of galaxy sample selection and then the bar identification methods applied are presented in Section 3. Section 4 contains the results: the evolution of the bar fraction from  $z = 1.3$  to  $z = 0.25$ . We perform a cursory dynamical analysis of individual galaxies in Section 5, and present two statistical analyses motivating the observed lack of bars. We note biases in our methods and the impact of galaxy substructure in Section 6. We then discuss the results in the context of observations and other numerical simulations in Section 7, summarising and concluding in Section 8.

## 2 SIMULATION AND GALAXY SELECTION

### 2.1 New Horizon simulation

The simulation sample studied in this paper is taken from the high-resolution hydrodynamical cosmological zoom-in simulation NEWHORIZON, a detailed description of which is presented in Dubois et al. (2021). The parent HORIZON-AGN simulation (Dubois et al. 2014), with box size of 142 Mpc, successfully reproduces galaxies in the various cosmic environments with a reasonable morphological mix (e.g. Dubois et al. 2016; Kaviraj et al. 2017; Martin et al. 2018), with thin and thick disks with scale heights and luminosity ratios as observed (Park et al. 2021). However, due to its limited

spatial and stellar mass resolution ( $\sim 1$  kpc and  $2 \times 10^6 M_{\odot}$ , respectively), it is not well suited to study detailed structures of galaxies such as bars. The NEWHORIZON simulation resimulates a sphere with a radius of 10 Mpc from HORIZON-AGN with a dark matter (DM) mass resolution of  $1.2 \times 10^6 M_{\odot}$  (compared to  $8 \times 10^7 M_{\odot}$  in HORIZON-AGN), a stellar mass resolution of  $1.3 \times 10^4 M_{\odot}$  (compared to  $2 \times 10^6 M_{\odot}$  in HORIZON-AGN) and a maximum spatial resolution of 34 pc (compared to 1 kpc in HORIZON-AGN). The exquisite resolution makes this simulation ideal for studying inner sub-structures within galaxies such as bars.

NEWHORIZON adopts a  $\Lambda$ CDM cosmology compatible with the WMAP-7 data (Komatsu et al. 2011) with cosmological parameters: Hubble constant  $H_0 = 70.4 \text{ km s}^{-1} \text{ Mpc}^{-1}$ , total mass density  $\Omega_m = 0.272$ , total baryon density  $\Omega_b = 0.0455$ , dark energy density  $\Omega_{\Lambda} = 0.728$ , amplitude of power spectrum  $\sigma_8 = 0.809$ , and power spectral index  $n_s = 0.967$ .

Dubois et al. (2021) describe in detail the simulation techniques employed and present several key fundamental properties of simulated galaxies including the galaxy mass function, the cosmic star formation rate, the galaxy sizes, their stellar kinematics, morphology and their evolution with redshift that are broadly in agreement with the literature.

### 2.2 Galaxy Selection

Galaxies are identified and extracted from the NEWHORIZON simulation using either the AdaptaHOP (Aubert et al. 2004) or the HOP (Eisenstein & Hut 1998) galaxy identification algorithm. The latter keeps all the substructures (i.e. star forming clumps and connected satellites) in a galaxy whereas the former removes the majority of these substructures. The AdaptaHOP selected galaxies will be the primary focus of this analysis, however, HOP galaxies will also be studied and discussed in Section 6.2.

To study bars across a wide range of masses, we select a minimum galaxy mass of  $M_{\star} \geq 10^{7.25}M_{\odot}$  (see also Dubois et al. 2021) resulting in 525, 479, 416, 381 and 299 galaxies above this mass cut at redshifts 1.3, 1.0, 0.7, 0.5 and 0.25, respectively<sup>1</sup>. A discussion on galaxy and halo identification, as well as the number of galaxies for different stellar mass thresholds identified, can be found in Section 2.6 of Dubois et al. (2021).

The bar fraction is defined in terms of spiral galaxies. Therefore, disc-dominated (spiral) galaxies must be distinguished from spheroidal-dominated (early-type) galaxies. We do this using stellar kinematics of galaxies as a proxy to infer a galaxy's morphology. We first find the spin of a galaxy by measuring its angular momentum vector from the velocity vectors of its stars. This spin vector defines the orientation of the  $z$ -axis cylindrical coordinate system to which the Cartesian coordinates of each stellar particle are transformed. The rotational velocity  $V$  of the galaxy is the average of the tangential velocity component. The velocity dispersion  $\sigma = \sqrt{(\sigma_r^2 + \sigma_t^2 + \sigma_z^2)/3}$ , where  $\sigma_{r,t,z}^2 = \langle V_{r,t,z}^2 \rangle - \langle V_{r,t,z} \rangle^2$ , with the subscripts  $r, t, z$  indicating the radial, tangential and vertical components, respectively. The ratio  $V/\sigma$  then provides an insight into the morphology of a galaxy. We use this parameter to select a sample of disc (rotation-dominated) galaxies, by adopting  $V/\sigma > 0.5$ , consistently with the criterion used in Dubois et al. (2021)<sup>2</sup>. Our conclusions do not change when a higher threshold is

<sup>1</sup> The mass cut corresponds to a minimum of 2000 stellar particles.

<sup>2</sup> A similar cut also reproduces the observed disc/elliptical fraction trends in the HORIZON-AGN simulation (see Martin et al. 2018).

used. The kinematics are computed on stellar particles, AdaptaHOP or HOP, depending on the catalogue used, extracted within two effective radii ( $R_{\text{eff}}$ ; obtained from the half-mass radius of a galaxy, see [Dubois et al. 2021](#) for more details). The resulting fractions of spiral galaxies at all analysed redshifts are shown in Table 1.

### 3 BAR ANALYSIS

Visual analysis of the surface density of galaxies has long been standard practice in observational studies for both morphological classification of galaxies and the identification of bars, spirals and other stellar structures (see [de Vaucouleurs 1963](#); [Sandage 2005](#); [Nair & Abraham 2010](#); [Buta et al. 2010](#); [Masters et al. 2011](#), for both seminal works and for more recent innovations). However, visual inspection may suffer from ambiguity as to what constitutes a bar feature. Therefore, algorithmic surface density decompositions, such as Fourier analysis, are a natural step to ensure reproducibility.

We will employ here two different algorithmic bar detection methods relying on Fourier analysis. The first method (presented in Section 3.1) is based on an azimuthal spectral analysis of the stellar surface density of the galaxy ([Kraljic et al. 2012](#)), while the second (described in Section 3.2) relies on a harmonic decomposition of the velocity profile of the galaxy ([Petersen et al. 2019a](#)). We will see that comparing the two methods alongside inspecting galaxies visually produces a more robust measurement of the bar fraction than either method alone.

#### 3.1 Surface Density Harmonic Decomposition

The first bar detection method is presented in detail in [Kraljic et al. \(2012\)](#) and involves the azimuthal spectral analysis of the surface density of galaxies. In brief, we compute the stellar surface density of the galaxy, perform a fast Fourier transform (FFT) and analyse the Fourier components.

We compute the stellar surface density of the galaxy in the face-on projection (with the spin axis of the entire stellar content of the galaxy being used to define the corresponding line of sight). We take the size of the radial bins to be 100 pc so as to incorporate a few resolution elements, reducing the noise when calculating the Fourier phase. We then decompose the stellar surface density into Fourier components in the form

$$\Sigma(r, \theta) = \Sigma_0(r) + \sum_m A_m(r) \cos(m\theta - \Phi_m(r)), \quad (1)$$

where  $\Sigma(r, \theta)$  is the stellar surface density,  $\theta$  is the azimuthal angle, and  $r$  is the radial distance.  $A_m$  and  $\Phi_m$  are the associated Fourier amplitude and phase, respectively.  $\Sigma_0(r)$  is the azimuthally averaged profile of the stellar surface density. A typical signature of a bar being present in a galaxy is the prominence of even Fourier components, especially the  $m = 2$  mode. This bar identification process studies the Fourier phase  $\Phi_2(r)$ , which is constant with radius within the ‘bar region’ when a bar is present (as opposed to the spiral arm of a galaxy whereby  $\Phi_m$  would vary linearly with radius). For a bar to be present,  $\Phi_2(r)$  is allowed to vary over a given range within  $\pm 5^\circ$  around the median value (see [Kraljic et al. 2012](#)).

To ignore variations caused by central structure, the bar search started at a radius of 0.5 kpc (the inclusion of sub-kpc bars is intentional as observations point to their important contribution to the overall population; e.g. [Erwin 2018](#), although we note that our results do not change if we instead start at 1 kpc). This search for

the start of the bar region stopped at a radius of 2 kpc if no bar was found, as typically no bar identified visually starts its region of constant  $\Phi_2(r)$  at larger radii (e.g. [Masters et al. 2011](#); [Melvin et al. 2014](#); [Díaz-García et al. 2016](#)). The cutoff in the bar length is determined mainly by the resolution. Spiral arms typically have variations in  $\Phi_2$  of a few tens of degrees over a distance of a few kpc but can appear constant over a short distance. Because of this, it was decided that the bar region had to cover at least 1000 pc in order to exclude the structure of any spiral arms. We show in Section 4.2 that relaxing this constraint on the minimum length of the bar does not impact the bar fractions.

This Fourier analysis is highly dependent on accurately finding the centre of the galaxy as when the FFT is performed, the bar search procedure starts at the origin which is supposedly the centre of mass of the galaxy. However, for cases where the origin is slightly off-centre due to substructures (more apparent in HOP selected galaxies as opposed to the AdaptaHOP which removed the majority of these), the bar search procedure will not find any bars or structure. A detailed example and insightful discussion of an off-centred stellar bars is presented in [de Swardt et al. \(2015\)](#). To resolve for this, a shrinking sphere approach was used to effectively zoom in on the centre of the galaxy i.e. the centre of mass was first calculated within a sphere encompassing all stellar particles, the radius of this sphere was decreased by a factor of two and the centre of mass within this new sphere was calculated. The radius of the sphere was halved again and the process was repeated until the centre of mass position was consistent to a factor of  $10^{-5}$  across three iterations. This process proved to visually find the centre of each galaxy and this correct centring was checked by plotting the  $m = 1$  mode Fourier amplitude against radial distance. The  $m = 1$  mode corresponds to lopsidedness. When centred correctly, the  $m = 1$  amplitude will be minimised at small radii<sup>3</sup>.

‘Fake’ bars, i.e., spheroid-dominated galaxies with moderately flattened central regions in their face-on projection (see [Kraljic et al. 2012](#), for more details), were dismissed by performing this harmonic decomposition on all three projections of the galaxy. For a given edge-on projection a disc will appear relatively flattened or ‘bar-like’ (i.e. constant  $\Phi_2(r)$ ). Therefore, a potential bar detected in the face-on projection had to be confirmed in both edge-on projections. However, this process proved to just be additional quality assurance on our results, as almost all spheroid-dominated galaxies were removed by the cut of  $V/\sigma$  described in Section 2.2; on average, only two ‘fake’ bars were removed by this process at each redshift sample.

Figure 1 shows an example of a ‘strongly barred’ NEWHORIZON galaxy at  $z = 1.3$ . The figure plots the Fourier phase  $\Phi_2$  as a function of radial distance (used to determine the bar region) along with the corresponding Fourier amplitudes. We also present the face-on projection of the stellar surface density used in the visual inspection. This is one of the clearest and strongest bars found in our sample - one can see the clear peaks in the  $m = 2$  and  $m = 4$  Fourier amplitudes within the bar region - and we confirm this to be a barred galaxy via the detection through our velocity method (described below and with associated plots also shown in Figure 1). In Figure 2, we present the corresponding plots for an unbarred NEWHORIZON galaxy at  $z = 0.25$  that is confirmed as such using the two methods.

<sup>3</sup> Further confirmation of our the validity of our centre-finding strategy comes from the well-defined rotation curves showing coherent rotation in all galaxies we study. See Section 5.2.

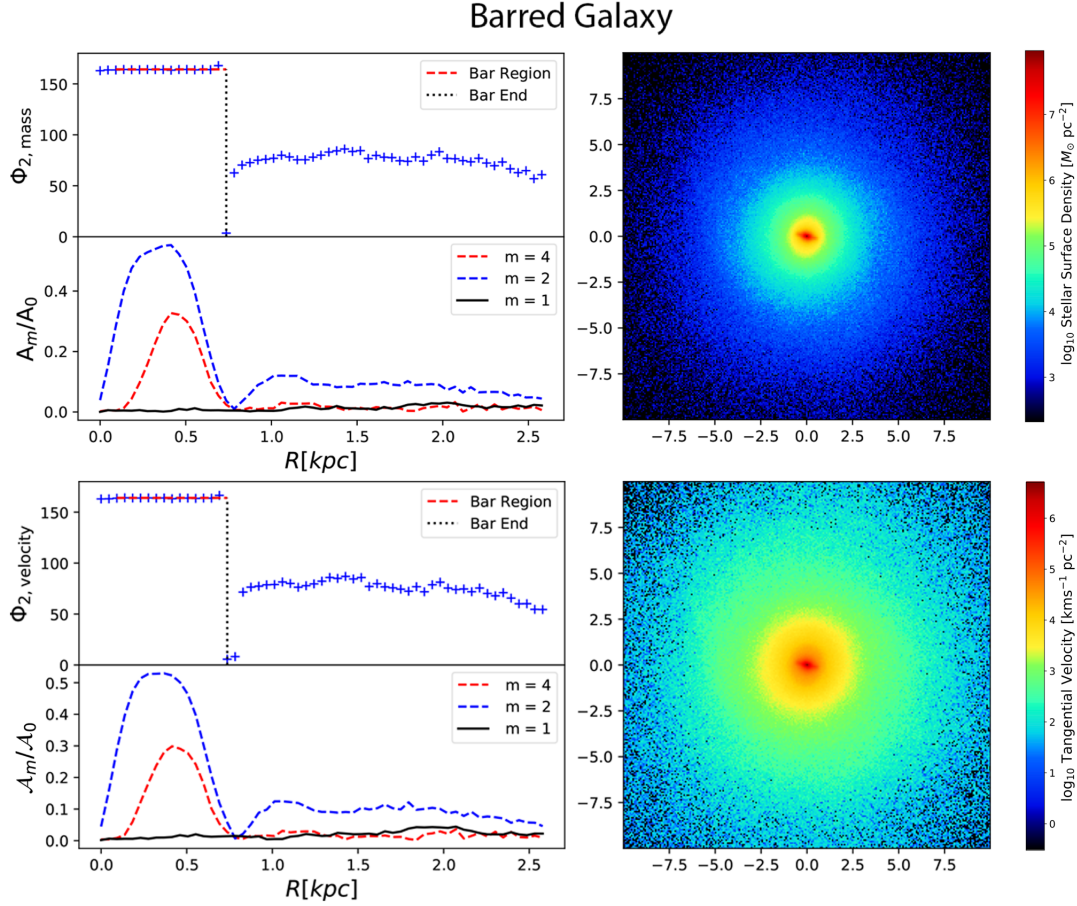


**Figure 1.** An example of our procedures used to detect a (strongly) barred NEWHORIZON galaxy at  $z = 1.3$ . Top row: detection of a bar region by the Surface Density Harmonic Decomposition method (Section 3.1). On the left, we present a plot of the Fourier phase  $\Phi_2$  weighted by stellar mass as a function of radial distance - as used to determine the bar region - along with the corresponding Fourier amplitudes. On the right, we show the stellar surface density face-on projected maps of the galaxy used for a visual inspection. Bottom row: corresponding plots for detection via the Velocity Harmonic Decomposition (Section 3.2). On the left, we present the plot of the Fourier phase  $\Phi_2$  weighted by tangential velocity as a function of radial distance along with the corresponding Fourier amplitudes. On the right, we show a face-on projection of the tangential velocity field of the galaxy which is used by the visual inspection of the stellar surface density for the surface density method. The surface density and velocity maps are plotted for  $20 \times 20 \text{ kpc}^2$  (but zoomed-in for clarity) and the colour coding scale is logarithmic.

### 3.2 Velocity Harmonic Decomposition

The second method for bar detection is inspired by the decompositions presented in Petersen et al. (2019a). Briefly, the method uses a velocity-weighted Fourier decomposition to identify coherent velocity signatures that are consistent with barred galaxies. The stellar particles that are part of the bar (the  $x_1$  orbit family as described in Petersen et al. 2021) dominate the velocity field, and these orbits create a detectable velocity signal that may be measured either in the average velocity field or (in the case of simulations) individual particle velocities.

Following the surface density harmonic decomposition of Section 3.1, we decompose the galaxy into Fourier components. However, we now compute the Fourier amplitude using a velocity field weighting, which we denote as  $\mathcal{A}_m$ . The velocity field  $\mathcal{V}$  is then decomposed as

$$\mathcal{V}(r, \theta) = \mathcal{V}_0(r) + \sum_m \mathcal{A}_m(r) \cos(m\theta - \Phi_m(r)), \quad (2)$$

as in equation (1).

The implementation of the method to the particle data starts the same way as in the primary method: the galaxy is first rotated

and centred using the method sketched in Section 3.1. The Fourier amplitudes  $\mathcal{A}_m$  are computed using the tangential velocity field. As in the surface density decomposition, we trace the Fourier phase  $\Phi_2(r)$  in radius to find a ‘bar region’ of constant phase. The requirements for detection are as in the surface density harmonic method ( $\Phi_2(r)$  must be constant within some radial range to  $\pm 5^\circ$  tolerance).

In our application, the bar search started at a radius of 0.5 kpc and the maximum start of the search for a bar was set at 2 kpc so as to mitigate variations caused by central structure. If the algorithm detects a region of constant Fourier phase  $\Phi_2(r)$ , it is flagged to be the putative bar region – only if the bar region covered at least 1 kpc. To ensure a particular peak in the Fourier amplitude was not noise induced, we require that the value of  $\mathcal{A}_2/\mathcal{A}_0$  at that particular radial distance remain above some threshold for significance. This threshold was set at  $\mathcal{A}_2/\mathcal{A}_0 > 0.02^4$ .

<sup>4</sup> To reduce the likelihood of contamination, one may lower this threshold. In our case, as we are using the velocity harmonic decomposition as a complement to the surface density harmonic decomposition, we do not take the indication of the presence of a bar as definitive proof, but rather as a candidate barred galaxy.

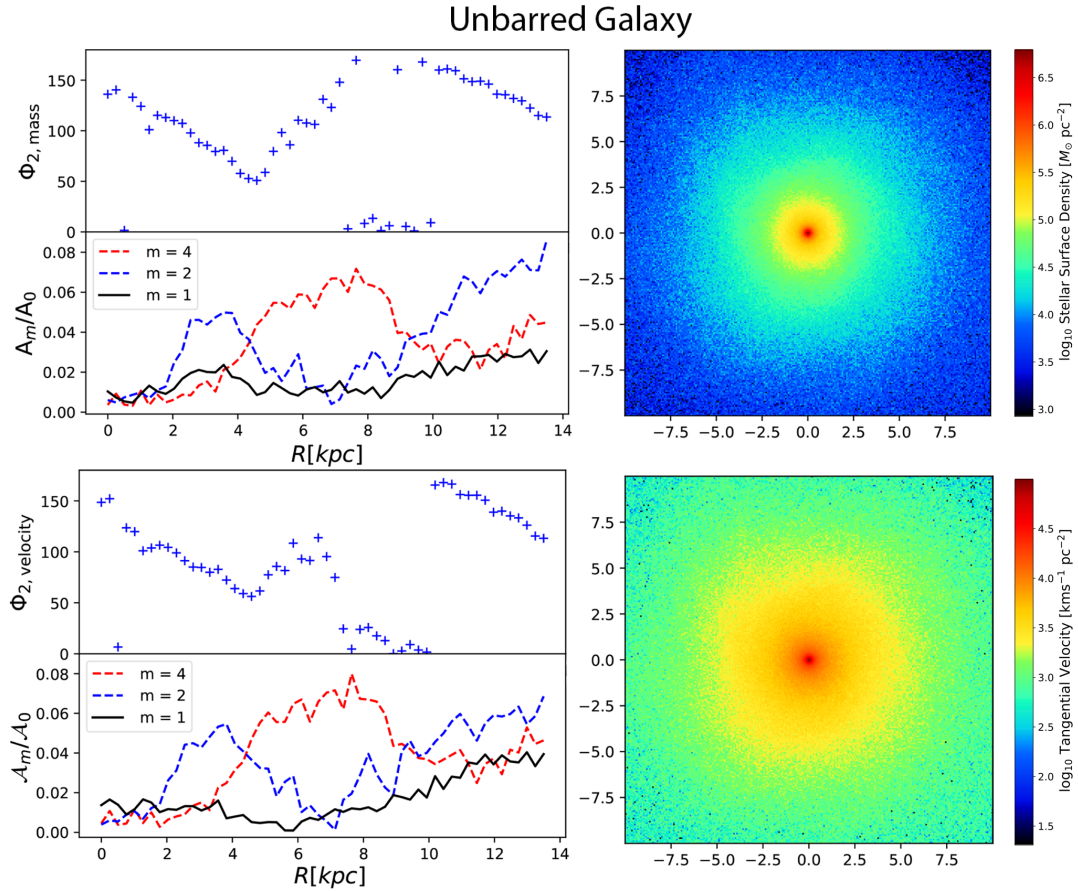


**Figure 2.** An example of the procedure applied to detect an unbarred NEWHORIZON galaxy at  $z=0.25$ . The format is the same as in Figure 1 whereby the surface density method is implemented in the top row, and the velocity method is shown in the bottom row. One can clearly see that this is an unbarred galaxy as there is no region of constant  $\Phi_2$  either weighted by stellar mass in the surface density method, nor weighted by tangential velocity in the velocity method. As in Figure 1, the surface density and velocity maps are plotted for  $20 \times 20 \text{ kpc}^2$  (but zoomed-in for clarity) and the colour coding scale is logarithmic.

Examples of this method used to detect both a strong barred NEWHORIZON galaxy at  $z = 1.3$  and an unbarred NEWHORIZON galaxy at  $z = 0.25$  are shown in Figures 1 and 2 respectively. In these figures, we plot Fourier phase  $\Phi_2$  weighted by tangential velocity as a function of radial distance - as used to determine the bar region - along with the corresponding Fourier amplitudes. We also show a face-on projection of the tangential velocity field of the galaxy which corresponds to the visual inspection of the stellar surface density for the surface density method. In Figure 1, the velocity harmonic decomposition behaves as expected: both  $\mathcal{A}_2$  and  $\mathcal{A}_4$  follow the expected bar signature profile, where  $\mathcal{A}_4$  peaks at the end of the possible bar while  $\mathcal{A}_2$  declines. In Figure 2, we see that the velocity harmonic profiles are not coherent in either  $\mathcal{A}_2$  or  $\mathcal{A}_4$ , which immediately rules out the presence of a bar.

### 3.3 Bar Strength

In order to provide a direct comparison with previous studies, we incorporate two methods to calculate bar strength widely used in the literature. The first is that of [Aguerri et al. \(1998\)](#), that is

$$S \equiv r_{\text{bar}}^{-1} \int_0^{r_{\text{bar}}} \frac{A_2}{A_0} dr, \quad (3)$$

where  $A_0$  and  $A_2$  are the zeroth and second mode Fourier amplitudes respectively and  $r_{\text{bar}}$  is the distance at which the  $A_2$  compo-

nent becomes comparable to the level of the higher order terms of the Fourier decomposition i.e. the outer radius of the bar region. The secondary proxy for bar strength (as used e.g. in [Díaz-García et al. 2016](#); [Rosas-Guevara et al. 2020](#); [Zhou et al. 2020](#)) is the maximum value of the ratio  $A_2/A_0$  ( $A_{2,\text{max}}$ ) within the bar region. In this paper, bar strengths are calculated using both methods, and have proven to give consistent results. Hereafter, the results presented use the integral definition (equation 3); however, these results do not change if  $A_{2,\text{max}}$  is used instead. In general, care should be taken when interpreting bar strength measurements, as some theoretical studies have suggested that bar strengths derived from Fourier measurements may not accurately quantify the effect of a bar on the evolution of the host galaxy (see, e.g. the comparison between apparent bar strength and the true bar potential in [Petersen et al. 2019a](#)).

Bars are classified depending on their bar strength,  $S$ , as follows;

- (i) *strong bars*, i.e. bars with a strength  $S \geq 0.3$  (consistent with [Kraljic et al. 2012](#)),
- (ii) *observable bars*, i.e. bars with a strength  $S \geq 0.2$ . This is the typical detection limit used in observations, when studying bars at high redshift ([Sheth et al. 2008](#))

We note that these definitions are somewhat arbitrary as there is a continuum of bar strengths ([Block et al. 2002](#); [Whyte et al.](#)

2002; Menéndez-Delmestre et al. 2007). We note also that the major results of this paper do not change if we alter these values. Any detection with strength  $S < 0.2$  is neglected as at this level, it is increasingly uncertain as to whether these are bars. This is mostly due to the perturbed nature of the larger mass galaxies or the limited resolution in the lower mass regime. These ensure that any visual inspection would be challenged to identify any barred structure (see Figure A1 where barred galaxies with strength only just greater than 0.2 are already unclear).

The strength measurement is relatively well-behaved when surface density decomposition is applied. However, the meaning of  $S$  is less certain in the velocity harmonic decomposition, and is likely strongly affected by noise (e.g. spatial resolution, particle number, and substructure fluctuations). That is, at low strength values, the false positive rate is substantial. We found that one must be particularly careful to cross-check low significance bars determined from the velocity harmonic decomposition with other methods.

#### 4 REDSHIFT EVOLUTION OF BAR FRACTION

The presence of a bar at increasing redshifts can indicate when galaxies have become dynamically cold and rotation dominated (Sheth et al. 2012). Furthermore, bars are one of the most frequently and easily quantified substructures in spiral galaxies, and hence, are often used as a tracer of galaxy evolution (Kraljic et al. 2012). A study of the redshift evolution of the bar fraction in galaxies therefore is a vital measurement when studying the evolutionary history of disc galaxies. We will now study the redshift evolution of the bar fraction in *NEWHORIZON*. The bar analysis has been carried out at redshifts  $z = 1.3, 1.0, 0.7, 0.5$  and  $0.25$ . Galaxy stellar masses range  $10^{7.25} M_{\odot} - 10^{11.04} M_{\odot}$  at  $z = 1.3$  and  $10^{7.28} M_{\odot} - 10^{11.38} M_{\odot}$  at  $z = 0.25$ . The errors represent  $1\sigma$  confidence intervals calculated using the (Bayesian) beta distribution quantile technique for estimating confidence intervals on binomial population proportions (Cameron 2011).

##### 4.1 Bar Fractions

Once the morphology of galaxies is determined, the bar detection methods, as described in Section 3, are applied to all the galaxies in the sample. If a galaxy is found to be barred, the length and strength of the bar are calculated whereby the length is simply two times the outer radius of the bar,  $r_{\text{bar}}$ , as described above. The measurements of the bar fractions for redshifts from  $z = 1.3$  to  $z = 0.25$  as calculated by both bar detection methods are shown in Table 1. If we compare these values to the 30%-70% measured from observational (e.g. Eskridge et al. 2000; Whyte et al. 2002; Laurikainen et al. 2004; Menéndez-Delmestre et al. 2007; Marinova & Jogee 2007; Barazza et al. 2008; Sheth et al. 2008; Aguerri et al. 2009; Nair & Abraham 2010; Masters et al. 2011, 2012; Melvin et al. 2014; Díaz-García et al. 2016) and from simulated (e.g. Athanassoula 2008, 2012; Zhou et al. 2020; Rosas-Guevara et al. 2020, 2021) studies, the disparity with our results is immediately obvious. *NEWHORIZON* produces substantially fewer barred galaxies than is expected based on the literature. But why is there such a large disparity? We will address this in Section 5 below.

The redshift evolution of the bar fraction is presented in Figure 3 for both ‘strong’ and ‘observable’ bars. From Figure 3, one can see that there is little evolution in the bar fraction with redshift, with only a slight decrease in strong and observable bar fractions with decreasing redshift. One can also see that while there is good

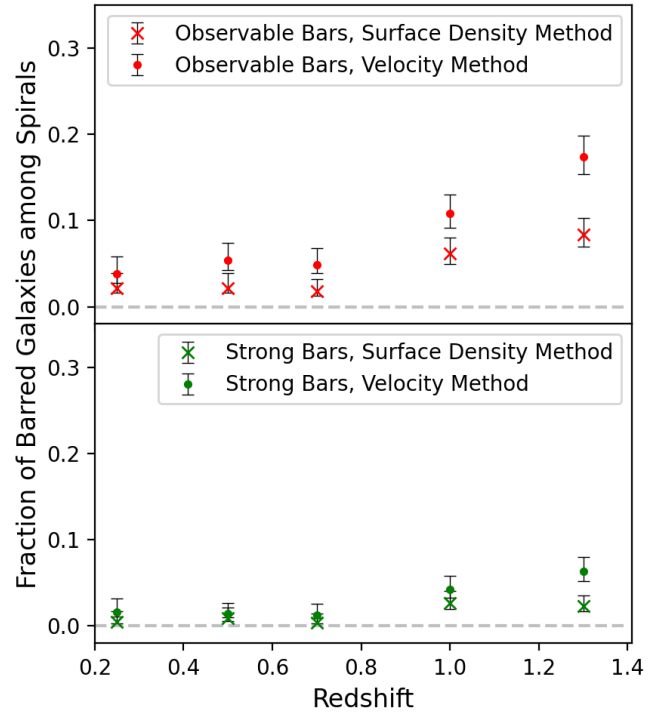


**Figure 3.** The redshift evolution of the bar fraction among disc-dominated galaxies across redshifts  $z = 1.3, 1.0, 0.7, 0.5$  and  $0.25$  calculated by both methods described in Section 3. The fractions from ‘observable bars’ are shown in the top panel those for ‘strong bars’ are shown in the bottom panel. One can see the agreement in bar fraction measurements between the two methods for ‘strong bars’ as well as the slight discrepancies for ‘observable bars’.

agreement in bar fractions between the two methods within the  $1\sigma$  errors, the velocity method appears to overestimate the observable bar fraction relative to the surface density method by 1-4%. Furthermore, on a galaxy-galaxy basis there is a disparity in those galaxies that are selected as barred by the two individual methods (in cases where the galaxy would not be identified as barred by eye). These discrepancies suggest that these two methods may produce ‘false positives’ whereby bar-like properties specific to each method are incorrectly classified as a bar. Therefore, a concurrence between the two methods is needed in order to confirm a galaxy as barred. Potential false positives will be analysed further in Sections 6.1 and 6.2 by analysing our sample on a galaxy-by-galaxy basis.

##### 4.2 Bar Properties

A typical property of bars studied in the literature is that of the bar strength as a function of galaxy stellar mass. In Figure 4 (top panels), we plot such a relationship at  $z = 1.3$  and  $0.25$  for bars detected using the Surface Density Harmonic Decomposition method. At  $z = 0.25$  we find a weak but statistically significant anti-correlation<sup>5</sup>, whereby more strongly barred galaxies tend to be in the lower mass regime while the higher mass galaxies tend to hold weaker bars. There is very little redshift evolution of this relation with a slight decrease in the number of detected bars. Similar trends are found if we perform our analysis on all the galaxies in the sample, not just

<sup>5</sup> Spearman coefficient of -0.335 with p-value=0.011

**Table 1.** The results of our analysis in terms of spiral fractions and bar fractions for ‘strong bars’ ( $S \geq 0.3$ ) and ‘observable bars’ ( $S \geq 0.2$ ) at redshifts  $z = 1.3, 1.0, 0.7, 0.5$  and  $0.25$ . The bar fractions as obtained by both bar detection methods described in Section 3 are shown. The confidence intervals presented have been estimated using the (Bayesian) beta distribution quantile technique (Cameron 2011). We also present numerical values in the parenthesis.

Redshift	Spiral Fraction (Number of Spirals)	Method	Bar Fractions (Number of Bars)	
			Strong Bars	Observable Bars
1.3	$0.570^{+0.021}_{-0.022}$ (299)	Surface Density	$0.023^{+0.012}_{-0.006}$ (7)	$0.084^{+0.019}_{-0.014}$ (25)
		Velocity	$0.063^{+0.017}_{-0.011}$ (19)	$0.174^{+0.024}_{-0.020}$ (52)
1.0	$0.543^{+0.023}_{-0.023}$ (260)	Surface Density	$0.027^{+0.014}_{-0.007}$ (7)	$0.062^{+0.018}_{-0.012}$ (16)
		Velocity	$0.042^{+0.016}_{-0.009}$ (11)	$0.108^{+0.022}_{-0.016}$ (28)
0.7	$0.538^{+0.024}_{-0.025}$ (224)	Surface Density	$0.004^{+0.010}_{-0.001}$ (1)	$0.018^{+0.014}_{-0.005}$ (4)
		Velocity	$0.013^{+0.013}_{-0.004}$ (3)	$0.049^{+0.016}_{-0.010}$ (11)
0.5	$0.580^{+0.025}_{-0.026}$ (221)	Surface Density	$0.009^{+0.012}_{-0.003}$ (2)	$0.027^{+0.016}_{-0.007}$ (6)
		Velocity	$0.014^{+0.013}_{-0.004}$ (3)	$0.054^{+0.020}_{-0.011}$ (12)
0.25	$0.581^{+0.027}_{-0.028}$ (183)	Surface Density	$0.005^{+0.012}_{-0.002}$ (1)	$0.022^{+0.017}_{-0.006}$ (4)
		Velocity	$0.016^{+0.016}_{-0.005}$ (3)	$0.038^{+0.020}_{-0.010}$ (7)

those selected as disc-dominated. And finally, comparable trends are found when using the Velocity Harmonic Decomposition method to detect bars, as shown in Figure C1. These points all seem to be indicative of i) there being very few strongly barred massive galaxies in NEWHORIZON and ii) there being some bias in the methods causing galaxies (that are not barred upon visual inspection - see Section 6.1) to be detected as barred.

In Figure 4 (bottom panels), we also plot the length of the detected bars against stellar mass. However we find that there is no clear dependence with mass for detected bars. This is in immediate disagreement with observations; Erwin (2018, 2019) in the local universe, Barazza et al. (2009) at intermediate redshift and Kim et al. (2021) out to  $z \sim 0.84$  all show a clear positive correlation between bar length and galaxy stellar mass. Again, we see little to no evolution in this relation with redshift, this time in agreement with Kim et al. (2021).

Our initial bar search criteria required a potential bar region to be at least 1 kpc in length before classifying the galaxy as barred. However, due to the spatial resolution of the NEWHORIZON simulation, we should expect to be able to resolve bars shorter than this. Despite this, by reducing this criterion on the bar length, we detect only one extra short bar (that having  $0.5 \text{ kpc} < \text{bar length} < 1 \text{ kpc}$ ) compared to longer bars (those with lengths  $> 1 \text{ kpc}$ ). This occurs when using the velocity method and is plotted in Figure C1 for completeness, demonstrating that our results do not change when allowing also for short bars.

In order to decipher the causes behind any biases in our bar detection methods, we will inspect galaxies visually as well as comparing detection methods on a galaxy-galaxy basis in Section 6. We will also compare our results in more detail to those of the literature

in Section 7 discussing their relevance and the lessons for future research. Let us now address the large disparity between our measured bar fractions and those of the literature - why the low bar fractions in NEWHORIZON and is there a missing bar problem in cosmological simulations?

## 5 A MISSING BAR PROBLEM?

While the biases that we will discuss in Section 6 may explain some discrepancies between measured bar fraction in observations and simulations, in particular at high redshift and/or at low stellar masses, the significant lack of bars in the NEWHORIZON simulation seems to point to a more fundamental problem.

Let us first discuss resolution effects in Section 5.1. We then present simple dynamical analysis of the disc galaxies at  $z = 1.3$  and  $z = 0.25$ . For each of the disc galaxies, we extract the gas and dark matter components within  $6R_{\text{eff}}$ . For galaxies above  $\log(M_{\star}/M_{\odot}) > 10.2$ , we extract the dark matter component out to  $30R_{\text{eff}}$  to account for the extended nature of these galaxies. We construct rotation curves, defining summary statistics (Section 5.2), and then analyse the sample of disc galaxies, making simple dynamical arguments for the low bar fraction (Section 5.3). We compute linear growth rates for composite models matching the population to quantify the dynamical state of the discs (Section 5.4).

### 5.1 Resolving secular processes

The resolution required to properly treat secular processes is not straightforward. In general, one may consider the role of both mass

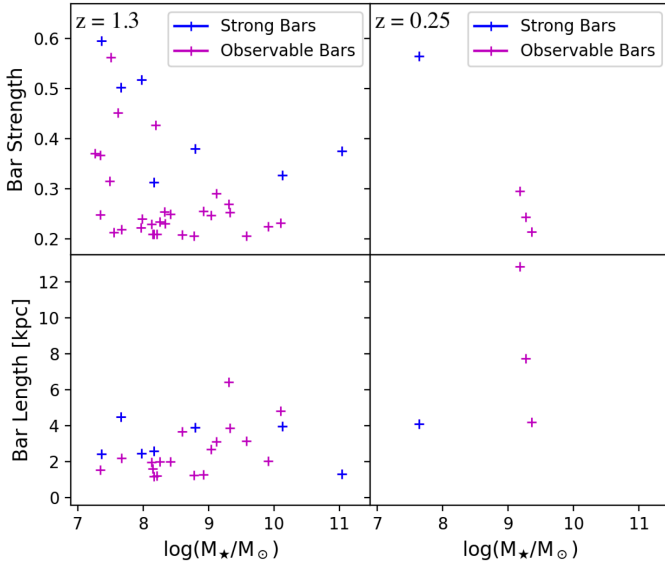


**Figure 4.** Figure showing bar strengths vs stellar mass (top panels) and bar lengths vs stellar mass (bottom panels) for  $z = 1.3$  (left panels) and  $z = 0.25$  (right panels). Bar strengths of both observable and strong bars are plotted for bars found in disc-dominated galaxies. One can see that there is only a very weak anti-correlation between bar strengths and galaxy stellar mass and almost no correlation for bar lengths. One can also see that there is almost no evolution in these trends with redshift. Furthermore, these trends are seen when plotting for bars detected in all the galaxies in the sample, not just those selected as disc-dominated – indicative of the possibility that some bias in the method causes certain galaxies to be detected as barred. These bars have been detected using the Surface Density Harmonic Decomposition method. A corresponding trend is found by the Velocity Harmonic Decomposition method and this plot is shown in Appendix C1 for comparison.

and spatial ‘resolution’ in cosmological simulations. Both are critical for correctly modelling secular processes, which can strongly be amplified by the disc’s temperature, should the disc’s thickness be resolved (Fouvry et al. 2015).

The mass resolution, or the number of particles, has been identified as a crucial ingredient for the accurate modelling of complex secular processes in galaxies such as bar formation, spiral arms or pseudo-bulges. For instance, by studying the details of resonant interactions, Weinberg & Katz (2007a) derived explicit criteria for the number of particles required to capture accurately these dynamical processes in N-body simulations. Typically, for a Milky Way-like galaxy,  $10^7 - 10^8$  particles are required to minimise the fluctuations in the gravitational potential so as to sufficiently populate regions near resonances. This should prove in particular relevant to model dynamical friction from the dark halo onto the bar. Yet modern simulations, and in particular zoom-in simulations, typically employ a number of particles that approaches this requirement (even though they might not correctly model the full disc dynamics; see Weinberg & Katz 2007b, for more discussion).

However, in the context of bar formation in cosmological simulations, spatial resolution appears to play a critical role. In a meta-analysis of the literature, the bar fraction in zoom-in simulations of Milky Way-like galaxies that have spatial resolution better than  $\sim 100$  pc is essentially zero. Some recent examples include, e.g. VINTERGATAN (Agertz et al. 2020) with a resolution of  $\sim 20$  pc, FIRE-2 (Hopkins et al. 2018), simulations of Nuñez-Castiñeyra et al. (2021),

or Galactica (Park et al. 2021) with a resolution comparable to that of NEWHORIZON.

Zoom-in simulations that manage to form bars typically choose lower spatial resolution, either motivated by ‘optimal’ softening length arguments (Power et al. 2003) or owing to mass resolution. For example, Zana et al. (2018) uses the softening length of 120 pc, the Auriga project (Grand et al. 2017; Blázquez-Calero et al. 2020) adopts the physical softening length for stars of 369 pc and for some older zoom-in simulations such as e.g. Scannapieco & Athanassoula (2012), it is 1.4 kpc for gas, stars and DM components, in Agertz et al. (2011), the maximum level of refinement reaches a physical resolution of 170 pc, and the simulations used in Kraljic et al. (2012) have the spatial resolution of 150 pc.

As will be discussed in Section 6.1, the most prominent barred galaxy at  $z = 1.3$  belongs to the most massive disc at that redshift<sup>6</sup>. Is this a coincidence? Given that this galaxy is found to be barred at  $z = 1.3, 1.0$  and  $0.7$ , it is highly unlikely that this detection is a statistical fluke. Thus, NEWHORIZON seems able to produce the conditions for bar formation under some circumstances. However, its presence cannot be fully explained by mass resolution: a more massive (and therefore equally high mass-resolution) disc is definitively unbarred at  $z = 0.25$ .

Finally, the (star formation recipe and resolution-dependent) number of massive clumps within the disc may impact the secular resilience of bars. This issue can be qualitatively addressed via the so-called Hamiltonian mean field model (Pichon & Lynden-Bell 1993; Antoni & Ruffo 1995). This involves computing orbital diffusion coefficients within the separatrix defined by the bar, using the Balescu-Lenard quasi-linear theory (Heyvaerts 2010; Fouvry & Bar-Or 2018), which captures the impact of the number of orbit-averaged clumps, given their relative contribution to the bar’s self-gravity. Benetti & Marcos (2017) compute these coefficients as a function of bar strength, and find (their figure 6) that i) below the separatrix, diffusion is fairly efficient for weak bar, while it is much less so for strong bars; ii) at the separatrix, the diffusion coefficient vanishes; iii) in the strong bar limit, wakes weaken diffusion (i.e. their Balescu-Lenard predictions versus Landau’s). While their setting is idealised, with a slightly different geometry, their results seem consistent with the naive expectation that a weaker bar will dissolve more easily through resonant encounters, whereas its strong counterpart will more easily sustain massive clump formation. It remains to be seen that i) the lifespan of these clumps is long enough for relaxation processes to operate, ii) the strength of resonant encounters (quantified by these diffusion coefficients) are sufficient for clumps to jump the separatrix and iii) the fraction of the bar’s mass they drag is enough to eventually dissolve the bar. More prosaically, the number and size of stellar clumps may vary with increased resolution or change in star formation modelling, which would artificially impact bar resilience.

In closing, whether the spatial resolution and/or the choice of softening length and subgrid physics in simulations plays a key role in the presence or absence of bars should be the topic of further investigations. In the next sections, we examine two summary statistics and connect them with known secular processes responsible for bar formation in order to probe alternative, physically motivated reasons for the lack of bars in NEWHORIZON.

<sup>6</sup> Given that the mass of stellar particles are the same, the galaxy therefore has the largest number of stellar particles – apparently near the regime Weinberg & Katz 2007a would suggest for resolving some secular processes.

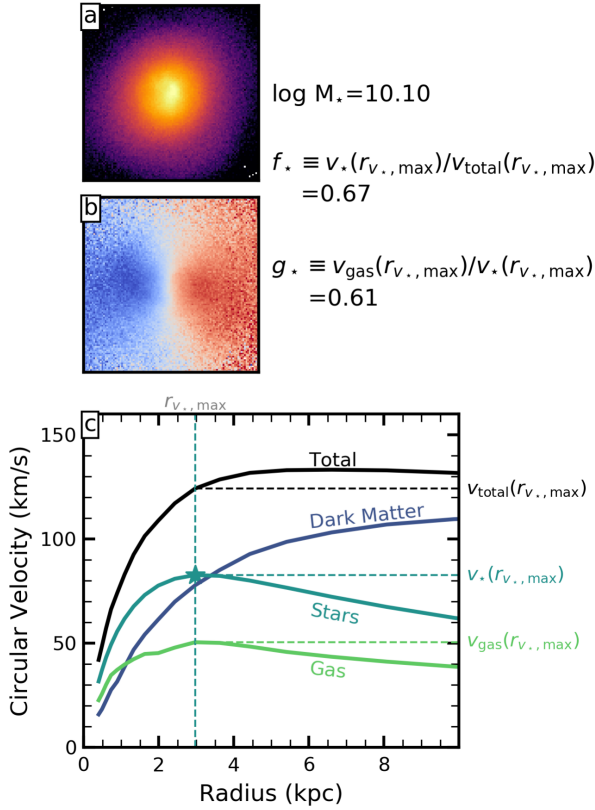


**Figure 5.** Face-on stellar surface density, velocity field, and rotation curve for an example galaxy at  $z = 0.25$ . The surface density resembles an exponential disc with a small bulge component. We also show the velocity field, which exhibits regular rotation. Panels a and b are 20 kpc per side. Panel c is the circular velocity curve, with listed and derived quantities as defined in the text. We show the total circular velocity curve in black, as well as the contributions from the dark matter, stellar, and gas components in coloured lines as marked. The location of the peak circular velocity contribution from the stellar disc is marked with a star.

## 5.2 Insights from rotation curves

One of the most straightforward ways to analyse the dynamics of a galaxy is through the rotation curve, or equivalently, the circular velocity curve. We construct the circular velocity curve from the mass enclosed ( $v_c(r) = \sqrt{GM(<r)/r}$ ) profile of the stellar, gas, and dark matter components, both separately and combined. While imperfect<sup>7</sup>, we find through visual inspection and comparison of the circular velocity to the measured mean tangential velocity of the disc stars that the circular velocity curves constructed through these naive means is satisfactory for dynamical inference. We will hereafter drop the ‘c’ subscript and refer to the circular velocity simply as ‘v’.

Figure 5 is a pedagogical demonstration of summary statistics we derive for each galaxy from the circular velocity curve. We define three key quantities in addition to the total stellar mass:

- (i) The radius at which the stellar contribution to the total circular velocity is maximised,  $r_{v_*,max}$ .
- (ii) The contribution to the total rotation curve by the stellar

<sup>7</sup> In particular, the assumption of a spherical distribution for the stellar and gas components introduces a small (up to 10%) bias in derived quantities.

component at  $r_{v_*,max}$ , which gives a measure of how ‘maximal’ the stellar component of a galaxy is,  $f_* \equiv v_*(r_{v_*,max})/v_{total}(r_{v_*,max})$ .

(iii) The ratio of the gas rotation curve value to the stellar rotation curve value at  $r_{v_*,max}$ , which gives a measure of the gas content in the galaxy relative to the stellar content,  $g_* \equiv v_{gas}(r_{v_*,max})/v_*(r_{v_*,max})$ .

In a pure exponential disc,  $r_{v_*,max}$  corresponds to  $2.2R_d$ , where  $R_d$  is the disc scale length. This is independent of the mass in the exponential disc,  $M_{disc}$ . The addition of a spherical bulge with mass  $M_{bulge}$  can alter the value of  $r_{v_*,max}$ : at fixed  $R_d$ , as the bulge fraction  $f_{bulge} \equiv M_{bulge}/(M_{bulge} + M_{disc})$  is increased,  $r_{v_*,max}$  decreases<sup>8</sup>. In the limit where  $f_{bulge} \rightarrow 1$ ,  $r_{v_*,max} \rightarrow 0$ . In practice,  $r_{v_*,max} = 0$  (where the bulge dominates the rotation curve of the galaxy) is achieved at  $f_{bulge} \gtrsim 0.35$ . When  $r_{v_*,max} \rightarrow 0$ ,  $f_*$  increases dramatically towards unity.

For  $f_*$  and  $g_*$ , we can draw insights from observational and theoretical literature for typical values that may promote secular bar formation. Local disc galaxies, including some hosting bars, exhibit  $f_{baryonic} \equiv f_*\sqrt{1+g_*^2} \in (0.4, 0.7)$ , with  $\langle f_{baryonic} \rangle = 0.57$  (Martinsson et al. 2013). As the majority of the galaxies in the Martinsson et al. (2013) sample have relatively low gas content<sup>9</sup>, a fair comparison for benchmarking to our simulations is  $f_* \approx f_{baryonic}$ . Athanassoula et al. (2013) found that increasing the gas content in isolated disc galaxies acted to slow the bar formation process, such that gas-dominated galaxies were near-axisymmetric for longer periods of time. Both linear stability studies (e.g. Pichon & Cannon 1997) and isolated simulations (Petersen et al. in prep) of disc galaxies indicate that at low  $f_*$ , bar formation is prohibited by the dominance of the dark matter halo. Conversely, when  $f_*$  is near unity owing to the presence of a large bulge driving the radius of the maximum of the stellar velocity curve to the centre of the galaxy, the galaxy dynamics may be stabilised against non-axisymmetric structure formation (Ambastha & Varma 1982). Taken together, we define a broad literature-derived space for ‘possible secular bar formation’ as  $0.4 < f_* < 0.8$  and  $g_* < 0.66$ .

## 5.3 Insights from the entire sample

Combining the summary statistics produces a four-dimensional space with the power to produce dynamical insights. In Figure 6, we show disc galaxies in the  $\log(M_*/M_\odot) - r_{v_*,max}$  plane at the highest redshift we consider ( $z = 1.3$ , left panel) and the lowest redshift we consider ( $z = 0.25$ , right panel). As in Jackson et al. (2021), we find that the dark matter content of the disc galaxies is in agreement with observations.

Through a linear regression analysis, we find a positive correlation between  $r_{v_*,max}$  (or  $R_d$ ) and  $\log(M_*/M_\odot)$  for galaxies with  $\log(M_*/M_\odot) < 9.5$  at both redshifts<sup>10</sup>. We interpret this relationship as a natural consequence of the galaxy formation process, where the scale length of the galaxy increases as the stellar mass of the galaxy increases through star formation. Indeed,

<sup>8</sup> Changing the geometry of the bulge, such as decreasing  $\alpha$  in a  $\rho_{bulge} \propto r^{-\alpha}$  bulge can also affect the location of  $r_{v_*,max}$  at fixed  $f_{bulge}$ , but in reasonable toy models we find this to be a second-order effect when compared to changing  $f_{bulge}$ .

<sup>9</sup> The maximum gas-to-stellar fraction (including both atomic and molecular gas) in this sample is 40%, which corresponds to  $g_* = 0.63$ .

<sup>10</sup> This partitioning of the sample is also degenerate with cuts on either  $f_*$  and  $g_*$ .

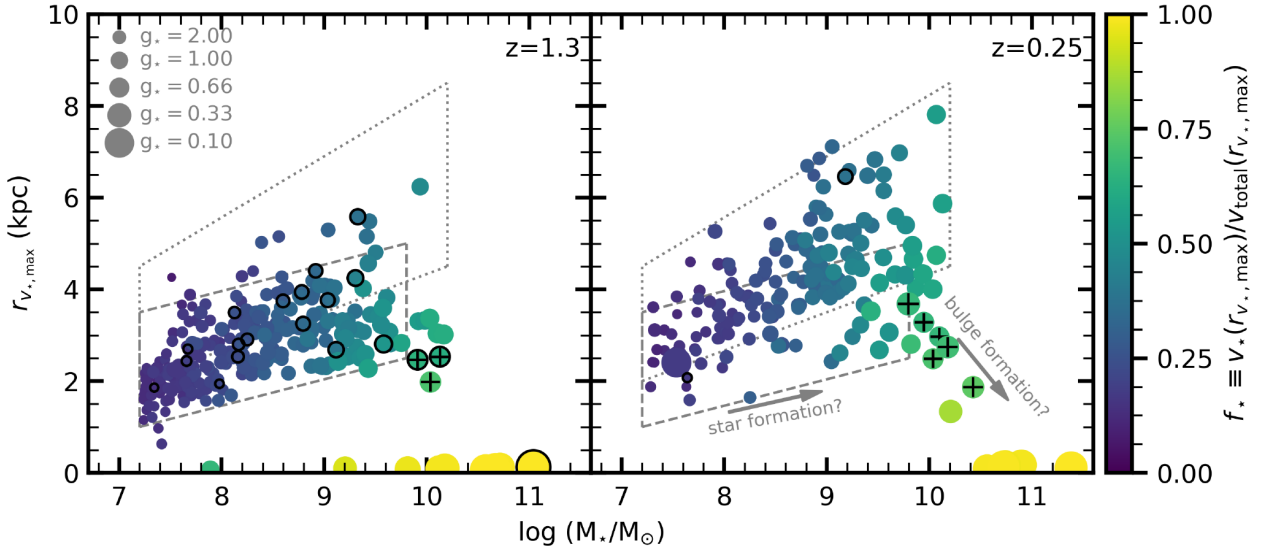


**Figure 6.** Two snapshots at different redshifts of disc galaxies in the  $\log(M_*/M_\odot) - r_{v_*,\max}$  plane. Colours correspond to  $f_*$ ; symbol sizes correspond to  $g_*$  (all quantities are defined in text). Galaxies identified as barred are outlined in black. Galaxies that fall in a region of ‘possible secular bar formation’ are indicated with a black ‘+’ ( $0.4 < f_* < 0.8$  and  $g_* < 0.66$ ). Most galaxies are excluded from the region of possible bar formation owing to either being relatively low stellar mass or by being bulge dominated. The left panel shows the highest redshift considered in this study,  $z = 1.3$ . The right panel shows the lowest redshift considered in this study,  $z = 0.25$ . Two possible evolutionary tracks are shown: first, star formation is expected to be responsible for the increase in  $r_{v_*,\max}$  with stellar mass. Second, bulge formation may be responsible for the dearth of galaxies with large  $r_{v_*,\max}$  at higher stellar masses. To guide the eye and easily follow the redshift evolution in this parameter space, in each panel we draw rough polygons around the bulk of the galaxies (dashed outline polygon corresponds to  $z = 1.3$ , dotted outline polygon corresponds to  $z = 0.25$ ).

a comparison of the two redshift snapshots suggests that galaxies generally increase  $r_{v_*,\max}$  (and thus scale length) while increasing mass. We also see generally increasing  $f_*$  and decreasing  $g_*$  from  $7 < \log(M_*/M_\odot) < 9.5$ .

However, above  $\log(M_*/M_\odot) = 9.5$ , a linear regression analysis finds a slight *negative* correlation between  $r_{v_*,\max}$  and  $\log(M_*/M_\odot)$  in the  $z = 0.25$  sample, and no correlation in the  $z = 1.3$  sample. Visual inspection of rotation curves indicates that this is a result of increasing  $f_{\text{bulge}}$ , towards the limit where the galaxy rotation curve peaks at small radii as a result of the presence of a bulge (the lower right corner of Figure 6). The apparent qualitative break from the positive trend seen at low mass ( $\log(M_*/M_\odot) \leq 9.5$ ) suggests that galaxies in NEWHORIZON may be in the process of forming large bulges above a certain mass threshold<sup>11</sup>. Evidently, some bulge formation proceeds at high redshift: several galaxies already exhibit prominent bulges by  $z = 1.3$ . We will study the formation and evolution of bulges in an upcoming work.

We mark the points of galaxies in Figure 6 that fall in the ‘possible secular bar formation’ regime defined above with black ‘+’ symbols. Of the sample of 128 (200) disc galaxies at  $z = 0.25$  ( $z = 1.3$ ), we find only *six* (three) that satisfy these criteria. Relaxing the  $g_*$  threshold to  $g_* < 1.0$  increases the number in the ‘candidate’ bar space dramatically (but does not capture any additional galaxies classified as barred in the sample). Widening the  $f_*$  range

to extend down to  $f_* > 0.3$  does not add any additional galaxies in the candidate bar space if  $g_*$  is held fixed. Visual inspection of the six  $z = 0.25$  galaxies classified as barred (including the galaxy in Figure 5) confirms that these galaxies are not barred, and prompts the question of whether the defined thresholds are too conservative: one explanation is that the actual bar-forming region in a theoretical  $f_* - g_*$  plane may be tighter than we conjecture above. One could also argue that  $r_{v_*,\max}$  as measured for disk galaxies in NEWHORIZON are unrealistic. However, this does not seem to be a plausible explanation as the effective radii (and therefore also the maximal radii) of NEWHORIZON galaxies are in a broad agreement with observations (see Dubois et al. 2021).

We mark the galaxies with detected bars (the putative bars as confirmed via a concurrence between our methods - see Section 6.1) in Figure 6 with black outlines. This results in 21 galaxies at  $z = 1.3$  and 2 galaxies at  $z = 0.25$ . The galaxies do not appear to preferentially reside in any region of the  $\log(M_*/M_\odot) - r_{v_*,\max}$  plane. None of the galaxies detected as barred at  $z = 1.3$  are detected as barred at  $z = 0.25$ . The formerly barred galaxies do not appear to have obviously undergone any ‘special’ evolution, or reside in a unique location in  $f_* - g_*$  space.

In particular, the defined ‘possible secular bar formation’ region in parameter space does not appear to hold any particular importance for NEWHORIZON galaxies. As the region is simply a space where isolated galaxy studies have previously identified bars, it does not preclude bar formation in regions outside of this space. The identification of bars in NEWHORIZON outside the possible secular bar formation region identified in isolated studies suggests that the bar formation in NEWHORIZON might be driven by different mechanisms than in isolated studies. We have little information about possible regions for bars triggered by interactions with other galaxies. Such a study is beyond the scope of this work, but cosmological simulations have a unique opportunity to explore bar formation be-

<sup>11</sup> Complicating our study and the relationship to previous works, the measurement of bulges in models is far from settled. Both kinematic (e.g. Park et al. 2021) and photometric (e.g. Blázquez-Calero et al. 2020) methods are regularly employed (and sometimes both, e.g. Gargiulo et al. 2019). While we have not attempted a detailed decomposition, the rotation curve in our model galaxies indicate significant central mass concentrations that set  $r_{v_*,\max}$ , which we refer to as ‘large bulges’.

yond the secular mode traditionally studied in bar dynamics. We conclude that the bars identified in *NEWHORIZON* do not resemble secularly formed bars as identified in previous studies of isolated galaxies.

#### 5.4 Insights from linear-response growth rates

Let us now present the trends from a linear response toy model tailored to provide insight into the lack of bars in *NEWHORIZON*. We follow Aoki et al. (1979), which studied the stability of razor thin, gaseous, isolated discs, while including varying bulge and halo components (see also Ambastha & Varma 1982). The construction of the model is detailed in Appendix D. The model is parameterised by four ratios:  $p = M_{\text{bulge}}/(M_{\text{disc}} + M_{\text{bulge}})$ ,  $q = M_{\text{disc}}/(M_{\text{disc}} + M_{\text{halo}})$ ,  $a_b/a_d$ , and  $a_h/a_d$ , where  $a_{\{b,d,h\}}$  are the scale lengths of the bulge, disc, and halo respectively and  $M_{\text{halo}}$  is the mass of the halo corresponding to the virial mass. With this parameterisation,  $a_d$  and  $M_{\text{disc}}$  may be readily scaled out. While galaxies in this model live in a four-dimensional space, we find it is reasonable for *NEWHORIZON* galaxies to reduce the four-dimensional space to a two-dimensional space parameterised by  $(p, q)$  by using typical values for  $a_b/a_d$  and  $a_h/a_d$  motivated by a mapping from the *NEWHORIZON* galaxies to the model (see Appendix D2).

We focus on linear instabilities possibly leading to bar formation: the bi-symmetric  $m = 2$  mode. Figure 7 plots the fastest growth rate,  $\omega_1$ , of a sequence of models parameterised by  $p$  and  $q$ , with  $a_b/a_d = 20$  and  $a_h/a_d = 2.8$ . Light (resp. dark) contours corresponds to slow (resp. fast) growth. The inverse of this growth rate quantifies the time it takes for a linear instability to grow (in units of the dynamical time). As seen on this figure, DM-dominated and bulge-hosting galaxies both have slow growth rates (lower right light region)<sup>12</sup>, unlikely to secularly grow strong non-linear bars, in qualitative agreement with the results in Section 5.3.

With the mapping derived in Appendix D2, we find that the bulge-less and bulge-hosting galaxies may be roughly split into distinct populations in  $(p, q)$  space. We therefore select ‘typical’ values to represent the two populations. We place an open galaxy symbol on Figure 7 at  $(\log p, \log q) = (-2, -1.7)$  representing the typical bulge-less galaxy in the sample at  $z = 1.3$ . We also place an open galaxy symbol at the location of the typical bulge-hosting galaxy at  $(\log p, \log q) = (-0.7, -1.0)$ . Comparing the bulge-less and bulge-hosting galaxies, we find that while the galaxies would be considered unstable with the modestly larger  $\log q$  values than the bulge-less counterparts, the bulge acts as a stabiliser when interpreted in the framework of this toy model. Interestingly, the most prominent barred galaxy at  $z = 1.3$  is by far the most massive disc in the  $z = 1.3$  sample, and lies at  $(\log p, \log q) = (-0.62, -0.34)$ , in a region where the bulge mass is too small for the bulge to stabilise the disc against bar formation. This galaxy is shown in Figure 1 and is shown as a filled galaxy symbol in Figure 7. However, tracking the same galaxy forward to lower redshift reveals that  $\log q$  decreases while  $\log p$  modestly increases, both of which would act to stabilise the galaxy against bar formation, and indeed, the observed bar is gone by  $z = 0.7$ .

At the level of this admittedly crude model, we show that nearly all *NEWHORIZON* discs fall in the linearly-stable part of parameter space, suggesting that secular processes alone, while adiabatically

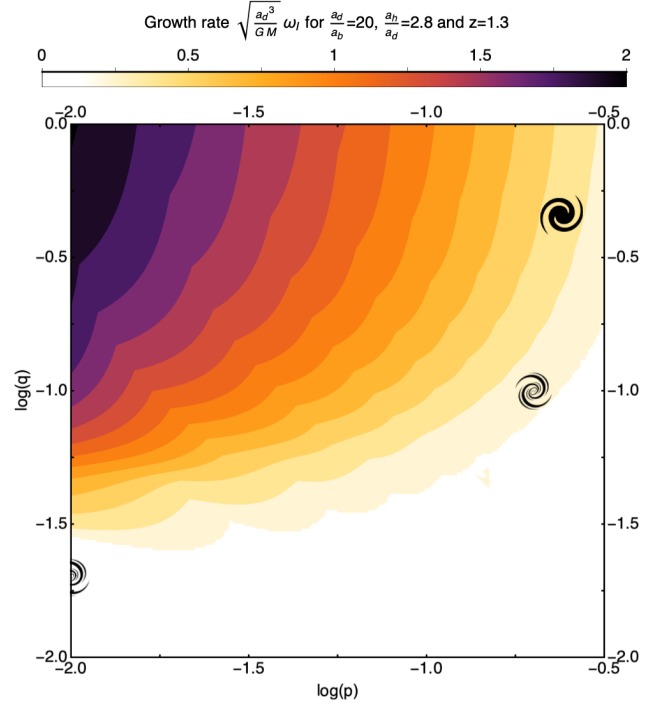


**Figure 7.** The fastest growth rate of  $m = 2$  modes in the Kuzmin-Toomre-Plummer fiducial model as a function of the two parameters,  $p$ , the bulge fraction, and  $q$ , the disc fraction for the quoted values of scale lengths. The bulge, disc and halo scale lengths are chosen to match those of *NEWHORIZON*. The completely white region corresponds to (ad hoc) values of  $\omega_1$  less than  $0.1\sqrt{GM/a_d^3}$ , which would lead to too slow bar mode growth. As a function of cosmic time, via accretion, star formation and mergers, the galaxies move within this diagram and may cross this threshold, triggering spontaneous bar formation. We place three representative points within the space: the bottom left represents a typical barless bulgeless galaxy, the central one a typical barless bulge-hosting galaxy, and the top one showing the approximate location of the most prominent barred galaxy in the sample at  $z = 1.3$ . The *NEWHORIZON* does not produce bi-symmetric unstable discs, with the exception of that one galaxy, which only hosts a bar for a fraction of a Hubble time.

changing the disc-to-halo and bulge-to-disc mass fractions and geometry, should not trigger bi-symmetric instabilities leading to bar formation.

These findings can be qualitatively explained either in an orbital alignment framework or a wave amplification one. In the former, the growing bulge (increasing  $p$ ) component deflects the alignment of elongated orbits which could build up the bar, while the lighter disc (decreasing  $q$ ) weakens the relative torques such tumbling orbits collectively apply on each other, preventing bar growth (Lynden-Bell 1979). In the latter, the growth of the bulge generates an inner Lindblad resonance which absorbs swing amplified waves (Goldreich & Tremaine 1978), breaking the amplification cycle towards bar growth. Conversely, the swing amplification is stronger in less dark matter dominated galaxies. The orbital formulation should also apply to the process of dissolving existing (non-linear) bar via cosmic gas infall, shepherded towards the centre by the bar, and building up a deflecting bulge.

The toy model highlights an alternative summary statistic space,  $(p, q)$  complementing that presented in Sec. 5.2, leading to an easily computed, physically motivated threshold for secular

<sup>12</sup> We set up a growth time threshold at a fraction,  $\eta$  of the dynamical time  $\sqrt{a_d^3/GM_\star}$  which, we somewhat arbitrarily set at  $\eta = 10$ . For a typical stellar mass of  $10^{10} M_\odot$  and  $a_d = 3$  kpc, this corresponds to 0.25 Gyr.

bar formation. It clearly does not allow to capture in full the realm of complex processes relevant to bar formation in general. For instance, beyond the aforementioned caveats, Aoki et al. (1979)'s formalism cannot rule out induced bar growth e.g. via strong tidal perturbations nor does it account for the impact of a live halo. Yet, within that framework, we can conclude that the measured bulge size and disc mass fractions explain the lack of bars in NEWHORIZON.

In conclusion, while the NEWHORIZON simulation has been shown to reproduce several key properties that define galaxies in reasonable agreement with observations, the sub-grid physics encoded in NEWHORIZON (and more generally in recent cosmological simulations resolving discs scale heights down to low redshifts, e.g. Hopkins et al. 2018; Agertz et al. 2020) seems to either lack resolution or induce a galactic assembly history statistically incompatible with secular bar formation. This 'bar problem' will need to be addressed in future work.

## 6 FALSE POSITIVES AND GALAXY SUBSTRUCTURE

In Section 4.1, we suggested that our two bar detection methods may produce 'false positives' whereby bar-like properties specific to each method are incorrectly classified as a bar and that therefore, a concurrence between the two methods is needed in order to confirm a galaxy as barred. In order to decipher the causes behind any biases in our bar detection methods, we will now inspect our galaxies visually as well as comparing detection methods on a galaxy-galaxy basis. We will then study further the impact that galaxy substructures have on bar detection in these methods.

### 6.1 A visual inspection on a galaxy-galaxy basis

An initial and rudimentary visual inspection of all the galaxies in our sample was carried out on the stellar mass surface density (face-on) projections of each galaxy. From this we find only *one* clear, elongated bar structure across the entire sample. This galaxy is presented in Figures 1 (stellar density) and 8 (mock images). It is also apparent that the galaxies in our samples are highly perturbed, even at  $z = 0.25$ , making any visual detection of smaller, more perturbed bars challenging. When applying the surface density method, we found that only  $\sim 2\%$  of galaxies hosted an observable bar (or  $\sim 1\%$  for "strong" bars) at redshifts  $z = 0.25, 0.5$  and  $0.7$  with this bar fraction increasing to 6 - 8% at redshifts  $z = 1.0$  and  $1.3$  (see Table 1). This highlights the complications involved in attempting to detect bars visually at high redshift due to the largely perturbed nature of these galaxies. Example grids of the most massive NEWHORIZON galaxies at  $z = 1.3$  and  $0.25$  are shown in Appendix B1 and B2 respectively to highlight their perturbed nature. When applying the velocity method to detect barred galaxies, we find there to be similar numbers of strong bars but slightly more observable bars in these samples.

Disparities in the specific galaxies selected as barred by each method suggest that in each of these methods, there is some bias producing 'false positives'. By comparing between the results in Tables 1 and 2 (described below), we see that across the full sample of galaxies, 1-2% of galaxies produce false positives in the surface density method and between 2-10% of galaxies produce false positives in the velocity method.

By inspecting these supposed barred galaxies in detail, both visually and with plots specific to the two bar detection methods, we find that the surface density method is actually picking out regions of constant phase in galaxies - either due to the galaxies being rather

**Table 2.** The final results of our bar search analysis in terms of bar fractions calibrated between the two methods whereby a barred galaxy is confirmed as such if said galaxy found to be barred in by both methods. The bar fractions (and number of barred galaxies) are shown for redshifts  $z = 1.3, 1.0, 0.7, 0.5$  and  $0.25$ . The confidence intervals presented have been estimated using the (Bayesian) beta distribution quantile technique (Cameron 2011) as in Table 1.

Redshift	Final Bar Fractions (Number of Bars)	
	Strong Bars	Observable Bars
1.3	$0.020^{+0.012}_{-0.005}$ (6)	$0.070^{+0.018}_{-0.012}$ (21)
1.0	$0.019^{+0.012}_{-0.005}$ (5)	$0.035^{+0.015}_{-0.008}$ (9)
0.7	$0.004^{+0.010}_{-0.001}$ (1)	$0.018^{+0.013}_{-0.005}$ (4)
0.5	$0.009^{+0.012}_{-0.003}$ (2)	$0.023^{+0.015}_{-0.006}$ (5)
0.25	$0.005^{+0.012}_{-0.002}$ (1)	$0.011^{+0.014}_{-0.003}$ (2)

perturbed or elongated due to galaxy-galaxy interactions or mergers or due to disordered structure in the central regions of the galaxy - where the stellar orbits are not actually aligned and trapped within a bar and so are not detected by the velocity method (which will be discussed more in Section 6.2 below). The velocity method also has its own bias whereby it finds some regions of aligned orbits as part of a 'bar region', but the very same region does not have a Fourier phase,  $\Phi_2$ , constant enough to be considered a bar by the surface density method.

This disagreement highlights strongly the difficulties in detecting bars, and the importance of cross-checking methods. Both detection methods give distinct false positives, as has become apparent in this study, due to the absence of many strong, elongated bars. For a robust detection, one can only confirm a galaxy as barred if both methods detect it as such. This cross-checking of two different detection methods (potentially coupled with a visual inspection - although less applicable at the low-mass end) is necessary then for studies of barred galaxies in the future.

By saying that, to confirm a galaxy as barred, the galaxy needs to be detected by both methods, we calculate final bar fractions as a result of concurrences between the methods and these are presented in Table 2. We present in Appendix A, for the reader's own visual inspection, face-on surface density projections of all the galaxies we confirm as barred. We stress here that our confirmation of a bar is based solely on agreements between the methods and that in this and the previous section, our 'barred' galaxies refers to these theoretical or putative bars. These 'bars' are rather perturbed and any visual inspection or observation would not be quick to suggest that these are, by any means, clear or certain bars. We can also see that, towards the low-mass regime, i.e.  $\log(M_*/M_\odot) < 8.0$ , it becomes increasingly difficult to identify any structure in the galaxy visually. In this regime, bar detection can only rely on our bar detection methods as any visual inspection will struggle to probe this mass range. These bars are often short-lived (only detected at their given redshift) and our overall finding of no clear, elongated bars found in NEWHORIZON remains consistent. The only exception is the galaxy presented in Figures 1 (stellar density) and 8 (mock images), which remains strongly barred from  $z = 1.3 - 0.7$  (see the first galaxy at each  $z = 1.3, 1.0$  and  $0.7$  in Figure A1). This is a fairly short (bar length  $\sim 1.3$  kpc), central bar but is the clearest and

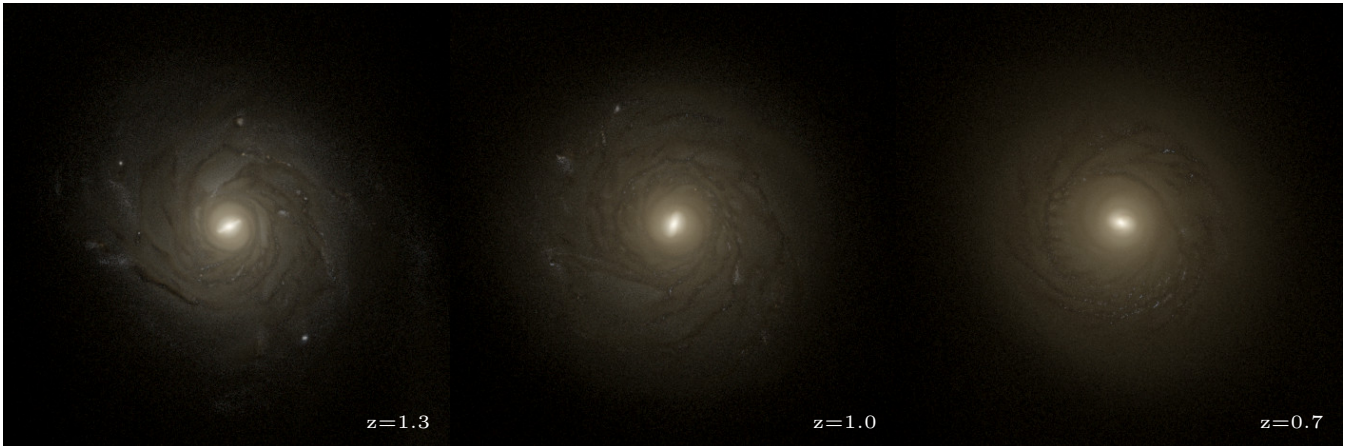


**Figure 8.** Mock observations of the only detected and visually confirmed barred galaxy at redshift  $z = 1.3$  (*left*),  $z = 1.0$  (*middle*) and  $z = 0.7$  (*right*). Mock images are produced face-on (with respect to the stellar angular momentum of the galaxy) in SDSS g-r-i bands using the SKIRT9 code (Camps & Baes 2020) that computes radiative transfer effects based on the properties and positions of the stars and the dusty gas, assuming a dust fraction of 0.4 following Saftly et al. (2015). Each panel has a size of 23.5 kpc across and the stellar mass of the galaxy is  $\sim 10^{11} M_{\odot}$ , with only a very weak evolution across this redshift range.

strongest detection of a barred galaxy we find and is the only bar that remains over multiple redshifts. The galaxy is also the most massive disc galaxy in the sample at  $z = 1.3$ ,  $\log(M_{\star}/M_{\odot}) = 11.04$ .

## 6.2 The impact of substructures on detection

Let us finally examine in more detail one bias that was brought up from the surface density method. That is disordered or clumpy substructure across the central regions of galaxies being detected as a bar. The galaxy identification algorithm AdaptaHOP as used in NEWHORIZON removes the majority of these substructures. However, the HOP identification algorithm keeps all these substructures and this is essentially how a galaxy would be analysed in an observational study if star forming clumps are not removed from these visual inspections. Because of this, and the fact that we know our detection method can produce false positives as a direct consequence of these clumps, let us study the effect of these on our measurements by studying galaxies identified using the HOP algorithm.

In order to determine the effects of these substructures in our bar detection method, we ran our analysis again but this time on galaxies identified using the HOP algorithm and compared to the results using AdaptaHOP. We found that there was very little difference between the HOP and the AdaptaHOP galaxies when using the velocity method at any redshift. Focusing on the surface density method, at the lower redshifts, there was very little difference in the bar fractions and in those galaxies selected as barred between the two galaxy identification algorithms. However, at  $z = 0.7$  and higher, where galaxies tend to be more clumpy and perturbed (see Martin et al. 2021, and their Figures 4 and 5 for a quantitative measure of morphological disturbances at different redshifts), we found an increase in the bar fractions with more galaxies being detected as barred. This allows us to quantify the effect that including galaxy substructures has on measurements of the bar fraction via the surface density method. These HOP bar fractions are shown in Table 3 for  $z = 0.7$  along with results of some previous studies for comparison.

As this surface density method relies on detected regions of roughly constant Fourier phase,  $\Phi_2$ , we see that bars can be identified in a galaxy as a direct consequence of aligned clumps across

the central region of a galaxy. As an example, we show in Figure 9 a clumpy galaxy at  $z = 0.7$  in which the surface density method detects a bar only when analysing the galaxy extracted using the HOP algorithm<sup>13</sup>. This highlights the potential problem with observing bars visually at high redshift, without the ability to perform a secondary, bar detection method. As the substructure of a galaxy cannot be easily removed from the observed images of galaxies, and given that galaxies at high  $z$  may be very perturbed, it is important to take into account a possible contamination by aligned stellar clumps that could be misidentified as bars.

To summarise, we observe an increase in bar fraction measured via the surface density method when analysing HOP galaxies. This is due to the detection of clumpy structure aligned within the central regions of a galaxy. Thus we caution that, without the ability to remove substructures or to easily invoke the secondary velocity method on observations (without integral field spectroscopy), our finding confirms that clumps may introduce some bias in the measurement of the bar fraction at high redshift, and highlights the importance of accounting for possible contamination by clumps.

## 7 THE LOW BAR FRACTION IN CONTEXT

In this section, we compare in more detail our measurements of the bar fraction to observations (Section 7.1) and simulations (Section 7.2), before discussing lessons learned for measuring bar fractions in both observations and simulations in Section 7.3.

### 7.1 Bar fractions measured from observations

While there is a general consensus that the fraction of barred galaxies in the local Universe is high (30%-70% depending on the bar classification method, the bar strength, the observed wave-bands and galaxy selection criteria Eskridge et al. 2000; Whyte et al. 2002; Laurikainen et al. 2004; Menéndez-Delmestre et al. 2007; Marinova

<sup>13</sup> We also examined the dark matter map of this galaxy and we confirm that these ‘clumps’ have no dark matter counterpart and therefore are real stellar clumps and not small, overlapping satellites.

**Table 3.** Table presenting the strong and observable bar fractions at redshift  $z = 0.7$  as obtained through the surface density method using the HOP galaxy selection algorithm alongside the results of one numerical and two observational studies. The definition of a strong bar is broadly in agreement across all of these works. One can see that the HOP results obtained here have increased by 1-3% compared to the previous AdaptaHOP results. This indicates that the presence of substructures may impact the bar identification and highlights the importance of carefully accounting for this effect, in particular at high redshift. The confidence intervals presented have been estimated using the (Bayesian) beta distribution quantile technique (Cameron 2011).

Type of Study	Strong Bar Fraction	Observable Bar Fraction	Reference
Simulation	$0.018^{+0.014}_{-0.005}$	$0.049^{+0.019}_{-0.010}$	This Work
Simulation	$\sim 0.1$	$\sim 0.2$	Kraljic et al. (2012)
Observational	$\sim 0.1$	-	Melvin et al. (2014)
Observational	$\sim 0.1$	$\sim 0.25$	Sheth et al. (2008)

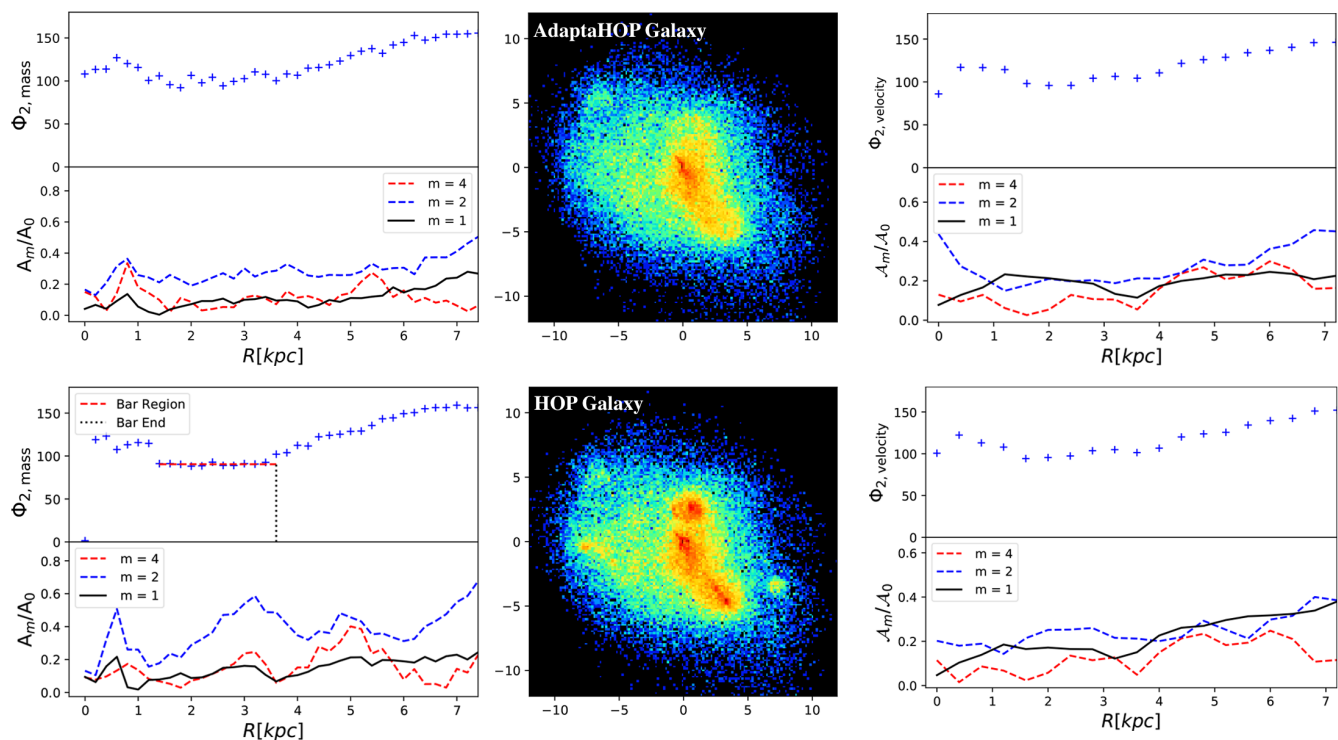


**Figure 9.** An example of a NEWHORIZON galaxy at  $z = 0.7$  that initially wasn't found to be barred in either method when the galaxy was selected using the AdaptaHOP algorithm. However, when selecting the galaxy using the HOP algorithm so as to include substructure, this galaxy was found to be strongly barred in the surface density method. Stellar density maps are shown on the middle panels along with the corresponding Fourier phase and amplitudes versus radial distance plots for the surface density method (left) and for the velocity method (right). The top panels show the galaxy as selected using the AdaptaHOP identification algorithm with the galaxy selected using the HOP algorithm so as to include the substructure shown in the bottom panels. The surface density method's bar search procedure has detected a region of roughly constant phase across the centre of the face on projection of the HOP galaxy. As this has only been detected when substructures have been included, we can conclude that this is indeed not a barred galaxy, but is in fact a result of aligned clumps across the central regions of the galaxy. This highlights the caution required when observing bars visually at high redshift without the ability to perform a secondary, velocity-based bar detection method.

& Jogee 2007; Barazza et al. 2008; Sheth et al. 2008; Aguerri et al. 2009; Nair & Abraham 2010; Masters et al. 2011, 2012; Melvin et al. 2014; Díaz-García et al. 2016), its stellar mass dependence is much more debated.

Erwin (2018) found, in the nearby ( $z < 0.01$ ) sample of spiral galaxies in the S<sup>4</sup>G survey, that the barred fraction ( $f_{\text{bar}}$ ) increases steeply from  $\sim 20\%$  at very low stellar mass ( $\sim 10^8 M_{\odot}$ ), reaching a maximum of  $\sim 76\%$  at  $M_{\star} \sim 10^{9.7} M_{\odot}$  before declining to  $50\%$  at  $M_{\star} \sim 10^{10-10.5} M_{\odot}$  and  $\sim 40\%$  at  $M_{\star} \sim 10^{11} M_{\odot}$ . These results are in broad agreement with another study of S<sup>4</sup>G galaxies (Díaz-García et al. 2016) reporting an increasing bar fraction from about

0%-15% (depending on the adopted method) for low mass ( $10^{8-8.5} M_{\odot}$ ) galaxies to 40%-60% at  $\sim 10^{9.5} M_{\odot}$ . Díaz-García et al. (2016) found that the fraction of bars then stays roughly constant out to  $10^{11} M_{\odot}$ . As suggested by Erwin (2018), this difference at high stellar masses can be attributed to selection criteria, mainly by the presence of S0 galaxies in the sample analysed by Díaz-García et al. (2016) producing a flat  $f_{\text{bar}}-M_{\star}$  trend. These measurements are in disagreement with most of the SDSS-based studies (e.g. Masters et al. 2012; Oh et al. 2012; Melvin et al. 2014) which report  $f_{\text{bar}}$  that increases strongly with stellar masses (for  $M_{\odot} > 10^{10} M_{\odot}$  typically). As shown by Erwin (2018), this is likely due to the

difficulty of SDSS-based studies to identify smaller bars at low stellar mass ( $< 10^{10} M_{\odot}$ ). The resulting underestimate of the bar fraction at these stellar masses leads to their incapability in tracing a peak in bar fraction at  $\sim 10^{9.7} M_{\odot}$ . A number of near infrared studies (e.g. [Díaz-García et al. 2016](#); [Erwin 2018](#)) also find that bar sizes depend on galaxy stellar mass – in the high mass regime,  $M_{\star} > 10^{10.2} M_{\odot}$ , bar length is found to increase with galaxy mass while lower mass galaxies tend to have bar lengths roughly constant at  $\sim 1.5$  kpc. This could suggest a limit on the size of bars one can resolve visually in these observational studies of lower mass galaxies with one possible explanation being that short bars could be missed when they coexist with a massive bulge ([Zhao et al. 2020](#)).

As opposed to the nearby Universe, measuring the bar fraction at higher redshifts proves to be increasingly difficult due to a lack of spatial resolution and band-shifting (see [Sheth et al. 2003](#)). But thanks to the high resolution deep optical and near-infrared data, it is today established that the fraction of barred galaxies decreases with increasing redshift (e.g. [Sheth et al. 2008](#); [Cameron et al. 2010](#); [Melvin et al. 2014](#); [Simmons et al. 2014](#)). These high redshift studies focus primarily on stellar masses above  $10^{10} M_{\odot}$  and find that  $f_{\text{bar}}$  i) increases with stellar mass from 15% (5%) for masses  $\sim 10^{10.3} M_{\odot}$  at  $z \sim 0.5$  (0.9) to  $\sim 35\%$  (10%) at  $10^{10.9} M_{\odot}$  at  $z \sim 0.5$  (0.9); ii) increases with time (from  $\sim 40\%$  at  $z \sim 0.25$  to  $\sim 10\%$  at  $z \sim 1$ ); or stays roughly constant for strong bars. Based on these observations, we expect there to be some evolution in  $f_{\text{bar}}$  with both mass and redshift in the high mass regime, and that the bar fraction in the low mass regime is low.

Clearly, the low bar fractions measured in NEWHORIZON (see Section 4.1) do not match the local sample of galaxies. The comparison is less obvious at higher redshift, but as our results are consistent with few bars in NEWHORIZON at any redshift, our findings are in tension with higher redshift observations as well. We do stress that we are probing, on average, a lower mass regime than Milky Way-mass local galaxies, or the mass regimes that are currently accessible in higher redshift observations (typically  $M_{\star} > 10^{10} M_{\odot}$ ). However, applying a similar stellar mass cut, i.e.  $M_{\star} > 10^{10} M_{\odot}$ , so as to make a more direct comparison to observations, does not change our conclusions. The fraction of strong and observable bars in NEWHORIZON galaxies above this mass cut is found to decrease from  $f_{\text{bar}} = 0.167$  at  $z \sim 1.3$  down to zero at  $z \sim 0.25$  (see Tables E1 and E2), in disagreement with both observed  $f_{\text{bar}}$  at low redshifts and its trend with cosmic time. Future space and ground-based facilities will be crucial for constraining bar fractions at increasing redshift.

## 7.2 Bar fractions measured in simulations

Large-scale cosmological simulations provide a powerful tool in studying the formation and evolution of bars. Recently, [Rosas-Guevara et al. \(2020\)](#), [Zhou et al. \(2020\)](#) & [Zhao et al. \(2020\)](#) present studies of barred galaxies in the TNG100 simulation. [Rosas-Guevara et al. \(2020\)](#) find a bar fraction of  $\sim 40\%$  at  $z = 0$  among the disc galaxies with stellar masses in the range  $10^{10.4-11} M_{\odot}$ . The fraction of barred galaxies is found to increase with stellar mass, more clearly for strong than for weak bars. The total bar fraction increases from 25% for the lowest to 75% for the highest stellar mass bin in their sample. They also find that strong bars tend to form in galaxies where a prominent disc component was established early (between  $0.5 < z < 1.5$ ) with more massive disc galaxies tending to host older bars whereas unbarred galaxies tended to form their disc components at later times. [Zhou et al. \(2020\)](#) present a comparison of the properties of bars between the ILLUSTRIS and the TNG100

simulations focusing mainly on the discrepancies between the two simulations as a result of star formation and AGN feedback. They find that, at  $z = 0$ , the fraction of bars among disc galaxies with stellar mass  $M_{\star} > 10^{10.5} M_{\odot}$  in TNG100 is 55% whereas in ILLUSTRIS it is 8.9%. The bar fraction increases with stellar mass in both simulations. In TNG100, it increases rapidly from 0% in the lowest stellar mass bin ( $10^{10.25-10.33} M_{\odot}$ ), to 30% in the intermediate mass bin ( $10^{10.50-10.58} M_{\odot}$ ), and to 50% in the range  $10^{10.66-11.25} M_{\odot}$ . In ILLUSTRIS, the bar fraction increases gradually from 0% in the stellar mass bin  $10^{10.50-10.58} M_{\odot}$ , to 10% for galaxies with  $M_{\star} \sim 10^{11} M_{\odot}$ , and then grows rapidly to 30%–40% for galaxies with  $M_{\star} > 10^{11.25} M_{\odot}$ , in agreement with [Peschken & Łokas \(2019\)](#), analysing the same simulation. The differences between these two simulations is suggested to be due to the combination of more effective stellar and AGN feedback in TNG100 which cause massive galaxies to have lower gas fractions at low redshifts, therefore aiding bar formation. Moreover, the work of by [Athanassoula et al. \(2013\)](#) indicates that gas-rich galaxies may indeed experience a delay in bar formation. By comparing galaxies directly between the ILLUSTRIS and the TNG100 simulations, [Zhou et al. \(2020\)](#) find that a galaxy’s morphology (and whether or not it is barred) at  $z = 0$  is dependent not only on the internal baryonic physics, but also on the environment - whether a galaxy experiences a merger, a flyby or solely secular evolution - which is often unpredictable. [Zhao et al. \(2020\)](#) also study bars in the TNG100 simulation, selecting galaxies with stellar masses  $M_{\star} \geq 10^{10} M_{\odot}$ . At  $z = 0$  the bar fraction is found to increase with stellar mass from  $\sim 5\%$  at stellar mass of  $10^{10} M_{\odot}$  up to  $\sim 75\%$  at  $M_{\star} \geq 10^{10.6} M_{\odot}$ , in disagreement with the observed almost constant bar fraction of 50%–60% over the same stellar mass range in the nearby Universe ([Erwin 2018](#)). When tracing the progenitors of  $z = 0$  massive galaxies (with  $M_{\star} > 10^{10.6} M_{\odot}$ ), they find an increasing bar fraction from 25% at  $z = 1$  to 63% at  $z = 0$ . Applying a constant mass cut of  $M_{\star} > 10^{10.6} M_{\odot}$  in the redshift range  $z = 0 - 1$  reveals instead a nearly constant bar fraction of 60%, while observations using a similar sample selection show a dramatic reduction of bars across the same cosmic epoch. They suggest that this discrepancy is due to the resolution of TNG100 and its inability to resolve bars with radii  $\leq 1.4$  kpc, as well as alluding to the possibility that observations may fail to identify many of these short bars at high redshifts.

[Rosas-Guevara et al. \(2021\)](#) study the evolution of the barred galaxy population in the recent TNG50 simulation. They focus on galaxies with masses  $M_{\star} > 10^{10} M_{\odot}$  and find a bar fraction of  $\sim 30\%$  at  $z = 0$  which evolves mildly to being above  $\sim 40\%$  at  $0.5 < z < 3$ . TNG50 is comparable to NEWHORIZON in terms of resolutions and volume and reproduces fairly well the cosmological evolution of the main properties of disc galaxies ([Pillepich et al. 2019](#); [Nelson et al. 2019](#)). While this high-resolution hydrodynamical simulation produces a bar fraction in rough agreement with observations at  $z = 0$ , they fail to reproduce the observed declining bar fraction at increasing  $z$  ( $> 0.5$ ).

The redshift evolution of barred galaxies have also been addressed by [Peschken & Łokas \(2019\)](#) in the ILLUSTRIS simulation, by analysing the evolution of high mass ( $M_{\star} > 10^{10.9} M_{\odot}$ ) disc galaxies. 21% of these are found to be barred at  $z = 0$ , while this fraction increases slightly with redshift. Most of these bars are triggered by external perturbations such as mergers or flybys, many of which disappear during secular evolution, leading to a lower bar fraction at present time compared to observations. Finally [Algorry et al. \(2017\)](#) examined disc galaxies with stellar masses in the range  $10^{10.6-11} M_{\odot}$  in the EAGLE simulations at  $z = 0$ , finding a total fraction bars of 40%, with 20% being strongly barred.

In summary, at  $z = 0$  all large-scale cosmological simulations seem to overproduce bars at high masses ( $M_{\star} \gtrsim 10^{10.5} M_{\odot}$ ) and tend to suppress their formation at low masses (in the stellar mass range  $M_{\star} = 10^{10-10.5} M_{\odot}$ ) compared to observations of the nearby Universe (Erwin 2018). These simulations also fail to reproduce the declining bar fraction with redshift, seen in most observations.

We stress again that the majority of previous studies, both observational (in particular at high redshift) and simulated, study larger mass galaxies due to the limited spatial resolution. Typically, they focus on galaxies with stellar masses  $M_{\star} > 10^{10-10.5} M_{\odot}$ , whereas the number statistics above this galaxy stellar mass in the NEWHORIZON simulation is low (see Table 1 of Dubois et al. 2021, for more details on galaxy masses within NEWHORIZON). Therefore, any comparison made to the literature in this section is not direct as this work presents an initial study into bars in low mass galaxies down to redshift  $z = 0.25$  owing to the higher spatial resolution of NEWHORIZON. However, as discussed in Section 7.1, when we limit our sample to galaxies with stellar masses  $M_{\star} > 10^{10} M_{\odot}$ , disagreement with these studies becomes even more striking, in particular at low redshift ( $z = 0.25$ ), where the bar fraction decreases to zero (see Tables E1 and E2). Stabilisation of these massive disks in NEWHORIZON against the formation of bars was further discussed in Section 5.

Future work is needed to measure bars homogeneously between simulations, for a homogeneous sample of simulated galaxies. We advocate using *both* methods employed in this work, which will eliminate spurious detections.

### 7.3 What are the lessons for bar fraction measurements?

The initial visual inspections of all galaxies extracted from the simulation showed that there was only one clear, strong, extended bar and that this bar was observed from  $z = 1.3$  to  $z = 0.7$  only. When applying a galaxy-by-galaxy comparison, we found disparities between the two methods: a detailed inspection revealed biases specific to each method (see Section 6.1) resulting in both methods giving false positives. This cross-checking of detection methods led to a final bar fractions of  $f_{\text{bar}} = 0.070$  at  $z \sim 1.3$  which decreases with decreasing redshift down to  $f_{\text{bar}} = 0.011$  at  $z \sim 0.25$  (see Table 2 for our full results), in disagreement with the majority of previous studies. Limiting our sample to galaxies with  $M_{\star} > 10^{10} M_{\odot}$  resulted in final bar fractions decreasing from  $f_{\text{bar}} = 0.167$  at  $z \sim 1.3$  to zero at  $z \sim 0.25$  (see Tables E1 and E2), in even stronger disagreement with previous studies at low redshift.

While these results may suggest a failure for the simulation to reproduce a striking feature of the observed Universe, it does highlight possible biases of observational studies of barred galaxies at lower mass and/or high  $z$  galaxies, and highlight the importance of robust detection methods.

Our initial bar search criteria required a potential bar region to be at least 1 kpc in length before classifying the galaxy as barred. By reducing this criterion to 0.5 kpc, we found virtually no change in our results. This, along with the perturbed nature and lack of visual clarity in the bars we detect, as well as bars being detected in lower mass galaxies all point to the increasing difficulty with which to confirm a bar visually as bars become shorter and more perturbed. These shorter bars are increasingly difficult to confirm as barred, owing to several reasons:

(i) When approaching the lower mass regime and/or when trying to resolve much shorter bars, we are approaching the limit of

application of the Fourier analysis to a surface density or a velocity field.

(ii) In the lower mass and short-bar regimes, the susceptibility of the two detection methods to noise in the determination of  $m = 2$  Fourier amplitude becomes a problem with the scale of the noisy regions becoming comparable to possible bar regions.

(iii) Both methods we employ are susceptible to producing false positives (e.g. regions of constant Fourier phase  $\Phi_2$ ). False positives are increasingly common if the minimum length criterion is reduced.

(iv) It is difficult to confirm short or weak bars visually, especially if these short bars coexist with a massive bulge or in lower mass galaxies where the structure of the galaxy.

Given our identified biases, which may be present in both observations and simulations, we highlight the difficulties involved in current observational estimates of bar fraction - whereby caution must be taken to exclude aligned stellar clumps or that shorter bars are unresolved - at high redshift and/or in the low-mass regime.

## 8 SUMMARY

We studied the redshift evolution of the bar fractions in galaxies extracted from the NEWHORIZON simulation at redshifts  $z = 1.3, 1.0, 0.7, 0.5$  and  $0.25$ . We selected 299, 260, 224, 221 and 183 disc galaxies at each respective redshift using the stellar kinematics of a galaxy as a proxy to infer its morphology. Galaxy masses ranged  $10^{7.25} M_{\odot} \leq M_{\star} \leq 10^{11.4} M_{\odot}$ , with only a handful (13 at  $z = 1.3$  and 21 at  $z = 0.25$ ) higher mass ( $M_{\star} \geq 10^{10} M_{\odot}$ ) galaxies in our sample. We implemented two bar detection methods - one based on the harmonic decomposition into Fourier components of the stellar surface density profile of the galaxy and the second based on the harmonic decomposition into Fourier components of the tangential velocity field of the galaxy - in order to provide a more robust measurement of the bar fraction. We then analysed galaxy rotation curves and growth rates to gain an insight into the measured low bar fractions and then studied biases that arose in the two methods and the impact of substructure in galaxies on bar fractions. The main results of our paper are as follows:

(i) A cursory dynamical analysis indicates that galaxies in NEWHORIZON may not reach thresholds in stellar content and distribution for bar formation. At lower masses ( $M_{\star} < 10^{10} M_{\odot}$ ), galaxies appear to be too dominated by dark matter relative to stellar content. At higher masses ( $M_{\star} > 10^{10} M_{\odot}$ ), galaxies appear to be stabilised by the presence of a central bulge.

(ii) We confirm barred galaxies as such by requiring detections in both methods. This results in final observable bar fractions of  $f_{\text{bar}} = 0.070^{+0.018}_{-0.012}$  at  $z \sim 1.3$  which decreases down to  $f_{\text{bar}} = 0.011^{+0.014}_{-0.003}$  at  $z \sim 0.25$ . This is in disagreement with the majority of past studies, both observational and numerical, namely large-scale cosmological simulations. Visual inspections of candidate barred galaxies revealed biases specific to each method, both giving false positives.

(iii) The measured bar fractions of disc-dominated galaxies in NEWHORIZON are too low compared to observational results reported in the literature. The most massive galaxies tend to host the weakest bars; there is little to no redshift evolution of the bar fraction, which all point to a challenge for current state-of-the-art galaxy formation models.

This work shows that the assembly history of the NEWHORIZON galaxies appears to quench the formation of any strong bars. It also highlights possible biases for observational studies of barred

galaxies at lower mass and/or high  $z$  galaxies, and highlights the importance of employing robust detection methods.

However, we stress that we are probing, on average, a lower mass regime than Milky Way mass local galaxies, or the mass regimes that are currently accessible to higher redshift observations. Future space-based observatories, such as with the James Webb Space Telescope, the Nancy Grace Roman Telescope, and other planned ground-based facilities will be crucial to constraining bar fractions at increasing redshift.

Beyond the scope of this paper, it would be interesting to track individual galaxies through cosmic time and study in details the evolution of their dark matter, gas and stellar components. This would help constraining further the parameters space favouring the formation of bars and eventually pin down *why* galaxies in *NEWHORIZON* do not appear to form bars. This will be addressed in the future work.

#### DATA AVAILABILITY

The data underlying this article will be shared on reasonable request to the corresponding author. The code of the linear stability analysis is available online at <https://github.com/KerwannTEP/LiRA>.

#### ACKNOWLEDGEMENTS

We thank Oscar Agertz and Florent Renaud for stimulating discussions. This work was granted access to the HPC resources of CINES under the allocations c2016047637, A0020407637 and A0070402192 by Genci, KSC-2017-G2-0003 by KISTI, and as a “Grand Challenge” project granted by GENCI on the AMD Rome extension of the Joliot Curie supercomputer at TGCC. This research is part of ANR Segal ANR-19-CE31-0017 (<http://secular-evolution.org>) and Horizon-UK projects. This work has made use of the Horizon cluster on which the simulation was post-processed, hosted by the Institut d’Astrophysique de Paris. We warmly thank S. Rouberol for running it smoothly. CP and KT thank J.B. Fouvry for numerous feedback. KK acknowledges support from the DEEPDIP project (ANR-19-CE31-0023). MSP acknowledges funding from a UK Science and Technology Facilities Council (STFC) Consolidated Grant. S.K.Y. acknowledges support from the Korean National Research Foundation (NRF-2020R1A2C3003769). RJ acknowledges support from the Yonsei University Research Fund (Yonsei Frontier Lab. Young Researcher Supporting Program) of 2021 and by the Korean National Research Foundation (NRF-2020R1A2C3003769). The supercomputing time for numerical simulation was kindly provided by KISTI (KSC-2017-G2-003), and large data transfer was supported by KREONET, which is managed and operated by KISTI.

#### REFERENCES

Abraham R. G., Merrifield M. R., Ellis R. S., Tanvir N. R., Brinchmann J., 1999, *MNRAS*, **308**, 569  
 Agertz O., Teyssier R., Moore B., 2011, *MNRAS*, **410**, 1391  
 Agertz O., et al., 2020, arXiv e-prints, p. [arXiv:2006.06008](https://arxiv.org/abs/2006.06008)  
 Aguerri J. A. L., Beckman J. E., Prieto M., 1998, *AJ*, **116**, 2136  
 Aguerri J. A. L., Méndez-Abreu J., Corsini E. M., 2009, *A&A*, **495**, 491  
 Algorry D. G., et al., 2017, *MNRAS*, **469**, 1054  
 Alonso S., Coldwell G., Duplancic F., Mesa V., Lambas D. G., 2018, *A&A*, **618**, A149

Ambastha A., Varma R. K., 1982, *Journal of Astrophysics and Astronomy*, **3**, 125  
 Antoni M., Ruffo S., 1995, *Physical Review E (Statistical Physics)*, **52**, 2361  
 Aoki S., Noguchi M., Iye M., 1979, *PASJ*, **31**, 737  
 Athanassoula E., 2002, *ApJ*, **569**, L83  
 Athanassoula E., 2008, *MNRAS*, **390**, L69  
 Athanassoula E., 2012, *MNRAS*, **426**, L46  
 Athanassoula E., Sellwood J. A., 1986, *MNRAS*, **221**, 213  
 Athanassoula E., Lambert J. C., Dehnen W., 2005, *MNRAS*, **363**, 496  
 Athanassoula E., Machado R. E. G., Rodionov S. A., 2013, *MNRAS*, **429**, 1949  
 Aubert D., Pichon C., Colombi S., 2004, *MNRAS*, **352**, 376  
 Barazza F. D., Jogee S., Marinova I., 2008, *ApJ*, **675**, 1194  
 Barazza F. D., et al., 2009, *A&A*, **497**, 713  
 Benetti F., Marcos B., 2017, *Physical Review E*, **95**, 022111  
 Berentzen I., Athanassoula E., Heller C. H., Fricke K. J., 2004, *MNRAS*, **347**, 220  
 Blázquez-Calero G., et al., 2020, *MNRAS*, **491**, 1800  
 Block D. L., Bournaud F., Combes F., Puerari I., Buta R., 2002, *A&A*, **394**, L35  
 Bournaud F., Combes F., 2002, *A&A*, **392**, 83  
 Bournaud F., Combes F., Semelin B., 2005, *MNRAS*, **364**, L18  
 Buta R. J., et al., 2010, *ApJS*, **190**, 147  
 Cameron E., 2011, *Publ. Astron. Soc. Australia*, **28**, 128  
 Cameron E., et al., 2010, *MNRAS*, **409**, 346  
 Camps P., Baes M., 2020, *Astronomy and Computing*, **31**, 100381  
 Cavanagh M. K., Bekki K., 2020, *A&A*, **641**, A77  
 Cheung E., et al., 2015, *MNRAS*, **447**, 506  
 Cisternas M., et al., 2013, *ApJ*, **776**, 50  
 Cisternas M., Sheth K., Salvato M., Knapen J. H., Civano F., Santini P., 2015, *ApJ*, **802**, 137  
 Combes F., Elmegreen B. G., 1993, *A&A*, **271**, 391  
 Combes F., Sanders R. H., 1981, *A&A*, **96**, 164  
 Debattista V. P., Sellwood J. A., 2000, *ApJ*, **543**, 704  
 Díaz-García S., Salo H., Laurikainen E., Herrera-Endoqui M., 2016, *A&A*, **587**, A160  
 Du M., Debattista V. P., Shen J., Ho L. C., Erwin P., 2017, *ApJ*, **844**, L15  
 Dubois Y., et al., 2014, *MNRAS*, **444**, 1453  
 Dubois Y., Peirani S., Pichon C., Devriendt J., Gavazzi R., Welker C., Volonteri M., 2016, *MNRAS*, **463**, 3948  
 Dubois Y., et al., 2021, *A&A*, **651**, A109  
 Eisenstein D. J., Hut P., 1998, *ApJ*, **498**, 137  
 Ellison S. L., Nair P., Patton D. R., Scudder J. M., Mendel J. T., Simard L., 2011, *MNRAS*, **416**, 2182  
 Elmegreen B. G., Elmegreen D. M., Hirst A. C., 2004, *ApJ*, **612**, 191  
 Erwin P., 2018, *MNRAS*, **474**, 5372  
 Erwin P., 2019, *MNRAS*, **489**, 3553  
 Eskridge P. B., et al., 2000, *AJ*, **119**, 536  
 Foreman-Mackey D., Hogg D. W., Lang D., Goodman J., 2013, *PASP*, **125**, 306  
 Fouvry J.-B., Bar-Or B., 2018, *MNRAS*, **481**, 4566  
 Fouvry J. B., Pichon C., Magorrian J., Chavanis P. H., 2015, *A&A*, **584**, A129  
 Fraser-McKelvie A., et al., 2020, *MNRAS*, **499**, 1116  
 Galloway M. A., et al., 2015, *MNRAS*, **448**, 3442  
 Gargiulo I. D., et al., 2019, *MNRAS*, **489**, 5742  
 Gerin M., Combes F., Athanassoula E., 1990, *A&A*, **230**, 37  
 Goldreich P., Tremaine S., 1978, *ApJ*, **222**, 850  
 Grand R. J. J., et al., 2017, *MNRAS*, **467**, 179  
 Guedes J., Callegari S., Madau P., Mayer L., 2011, *ApJ*, **742**, 76  
 Guo M., Du M., Ho L. C., Debattista V. P., Zhao D., 2020, *ApJ*, **888**, 65  
 Hasan H., Norman C., 1990, *ApJ*, **361**, 69  
 Hasan H., Pfenniger D., Norman C., 1993, *ApJ*, **409**, 91  
 Heyvaerts J., 2010, arXiv.org  
 Hohl F., 1971, *ApJ*, **168**, 343  
 Hohl F., 1976, *AJ*, **81**, 30  
 Hopkins P. F., et al., 2018, *MNRAS*, **480**, 800  
 Jackson R. A., et al., 2021, *MNRAS*, **502**, 1785

- Jogee S., et al., 2004, *ApJ*, 615, L105
- Kaviraj S., et al., 2017, *MNRAS*, 467, 4739
- Kim T., Athanassoula E., Sheth K., Bosma A., Park M.-G., Lee Y. H., Ann H. B., 2021, arXiv e-prints, p. arXiv:2109.03420
- Knapen J. H., Shlosman I., Peletier R. F., 2000, *ApJ*, 529, 93
- Komatsu E., et al., 2011, *ApJS*, 192, 18
- Kormendy J., 2013, Secular Evolution in Disk Galaxies. p. 1
- Kormendy J., Kennicutt Robert C. J., 2004, *ARA&A*, 42, 603
- Kraljic K., Bournaud F., Martig M., 2012, *ApJ*, 757, 60
- Laurikainen E., Salo H., Buta R., Vasylyev S., 2004, *MNRAS*, 355, 1251
- Lin L., et al., 2020, *MNRAS*, 499, 1406
- Lynden-Bell D., 1979, *MNRAS*, 187, 101
- Lynden-Bell D., Kalnajs A. J., 1972, *MNRAS*, 157, 1
- Marinacci F., Pakmor R., Springel V., 2014, *MNRAS*, 437, 1750
- Marinova I., Jogee S., 2007, *ApJ*, 659, 1176
- Martin G., Kaviraj S., Devriendt J. E. G., Dubois Y., Pichon C., Laigle C., 2018, *MNRAS*, 474, 3140
- Martin G., et al., 2021, *MNRAS*, 500, 4937
- Martinet L., Friedli D., 1997, *A&A*, 323, 363
- Martinsson T. P. K., Verheijen M. A. W., Westfall K. B., Bershadsky M. A., Andersen D. R., Swaters R. A., 2013, *A&A*, 557, A131
- Masters K. L., et al., 2011, *MNRAS*, 411, 2026
- Masters K. L., et al., 2012, *MNRAS*, 424, 2180
- Melvin T., et al., 2014, *MNRAS*, 438, 2882
- Menéndez-Delmestre K., Sheth K., Schinnerer E., Jarrett T. H., Scoville N. Z., 2007, *ApJ*, 657, 790
- Moetazedian R., Polyachenko E. V., Berczik P., Just A., 2017, *A&A*, 604, A75
- Nair P. B., Abraham R. G., 2010, *ApJS*, 186, 427
- Nelson D., et al., 2019, *MNRAS*, 490, 3234
- Noguchi M., 1987, *MNRAS*, 228, 635
- Núñez-Castiñeyra A., Nezri E., Devriendt J., Teyssier R., 2021, *MNRAS*, 501, 62
- Oh S., Oh K., Yi S. K., 2012, *ApJS*, 198, 4
- Okamoto T., Isoe M., Habe A., 2015, *PASJ*, 67, 63
- Ostriker J. P., Peebles P. J. E., 1973, *ApJ*, 186, 467
- Park M. J., et al., 2021, *ApJS*, 254, 2
- Peirani S., Hammer F., Flores H., Yang Y., Athanassoula E., 2009, *A&A*, 496, 51
- Peschken N., Lokas E. L., 2019, *MNRAS*, 483, 2721
- Petersen M. S., Weinberg M. D., Katz N., 2016, *MNRAS*, 463, 1952
- Petersen M. S., Weinberg M. D., Katz N., 2019a, arXiv e-prints, p. arXiv:1903.08203
- Petersen M. S., Weinberg M. D., Katz N., 2019b, *MNRAS*, 490, 3616
- Petersen M. S., Weinberg M. D., Katz N., 2021, *MNRAS*, 500, 838
- Pfenniger D., Norman C., 1990, *ApJ*, 363, 391
- Pichon C., Cannon R. C., 1997, *MNRAS*, 291, 616
- Pichon C., Lynden-Bell D., 1993, in Misquich J., Pelletier G., Schuck P., eds, Statistical Description of Transport in Plasma, Astro- and Nuclear Physics. p. 261
- Pillepich A., et al., 2018, *MNRAS*, 473, 4077
- Pillepich A., et al., 2019, *MNRAS*, 490, 3196
- Power C., Navarro J. F., Jenkins A., Frenk C. S., White S. D. M., Springel V., Stadel J., Quinn T., 2003, *MNRAS*, 338, 14
- Regan M. W., Mulchaey J. S., 1997, in American Astronomical Society Meeting Abstracts. p. 78.02
- Rosas-Guevara Y., et al., 2020, *MNRAS*, 491, 2547
- Rosas-Guevara Y., et al., 2021, arXiv e-prints, p. arXiv:2110.04537
- Saftly W., Baes M., De Geyter G., Camps P., Renaud F., Guedes J., De Looze I., 2015, *A&A*, 576, A31
- Sandage A., 2005, *ARA&A*, 43, 581
- Scannapieco C., Athanassoula E., 2012, *MNRAS*, 425, L10
- Schaye J., et al., 2015, *MNRAS*, 446, 521
- Sérsic J. L., Pastoriza M., 1965, *PASP*, 77, 287
- Shen J., Sellwood J. A., 2004, *ApJ*, 604, 614
- Sheth K., Regan M. W., Scoville N. Z., Strubbe L. E., 2003, *ApJ*, 592, L13
- Sheth K., Vogel S. N., Regan M. W., Thornley M. D., Teuben P. J., 2005, *ApJ*, 632, 217
- Sheth K., et al., 2008, *ApJ*, 675, 1141
- Sheth K., Melbourne J., Elmegreen D. M., Elmegreen B. G., Athanassoula E., Abraham R. G., Weiner B. J., 2012, *ApJ*, 758, 136
- Simmons B. D., et al., 2014, *MNRAS*, 445, 3466
- Stinson G. S., Brook C., Macciò A. V., Wadsley J., Quinn T. R., Couchman H. M. P., 2013, *MNRAS*, 428, 129
- Toomre A., 1963, *ApJ*, 138, 385
- Tremaine S., Weinberg M. D., 1984, *MNRAS*, 209, 729
- Ueda T., Noguchi M., Iye M., Aoki S., 1985, *ApJ*, 288, 196
- Vogelsberger M., et al., 2014, *MNRAS*, 444, 1518
- Wang J., et al., 2012, *MNRAS*, 423, 3486
- Weinberg M. D., 1985, *MNRAS*, 213, 451
- Weinberg M. D., Katz N., 2007a, *MNRAS*, 375, 425
- Weinberg M. D., Katz N., 2007b, *MNRAS*, 375, 460
- Whyte L. F., Abraham R. G., Merrifield M. R., Eskridge P. B., Frogel J. A., Pogge R. W., 2002, *MNRAS*, 336, 1281
- Zana T., Dotti M., Capelo P. R., Bonoli S., Haardt F., Mayer L., Spinoso D., 2018, *MNRAS*, 473, 2608
- Zana T., Capelo P. R., Dotti M., Mayer L., Lupi A., Haardt F., Bonoli S., Shen S., 2019, *MNRAS*, 488, 1864
- Zhao D., Du M., Ho L. C., Debattista V. P., Shi J., 2020, *ApJ*, 904, 170
- Zhou Z.-B., Zhu W., Wang Y., Feng L.-L., 2020, *ApJ*, 895, 92
- de Swardt B., et al., 2015, *ApJ*, 808, 90
- de Vaucouleurs G., 1963, *ApJS*, 8, 31
- van den Bergh S., 2011, *AJ*, 141, 188

## APPENDIX A: BARRED GALAXIES

As discussed in section 6.1, to confirm a barred galaxy as such, we required that a bar be detected via both methods applied. This was in order to remove any false positives produced by either method. In Figure A1, we present, for the readers interest and discussion, the surface density face-on projections of all the galaxies that we confirm as barred via this process at each redshift. It is clear that there are no clear, large, elongated bars in this simulation and that the bars detected here are mostly small and/or perturbed.

We remind the reader that our confirmation of a bar requires agreement between the methods and that our ‘barred’ galaxies refers to these theoretical or putative bars. These ‘bars’ are perturbed and that any visual inspection would not be quick to suggest that these are, by any means, clear or certain bars. These are often short-lived (only detected at their given redshift) and that our overall finding - no clear, elongated bars found in NewHorizon- remains consistent. The only exception is the galaxy presented in Figure 1, which remains strongly barred from  $z = 1.3 - 0.7$  (see the first galaxy at each  $z = 1.3, 1.0$  and  $0.7$  in Figure A1). This is a fairly short (bar length  $\sim 1.3\text{kpc}$ ), central bar but is the clearest and strongest detection of a barred galaxy we find and is the only bar that remains over multiple redshifts.

Some of the barred galaxies detected here are in the lower mass regime - towards the lower limit of the Fourier based methods where noise in the radial bins starts to become significant. These galaxies do not show clearly on these projections and suggest that in the very low mass range (below  $\sim 5 \times 10^7 M_{\odot}$ ), we are approaching the limit of bar detections via these methods in this simulation. These again further demonstrate the difficulties in observing bars at higher redshift and in the lower mass regime.

## APPENDIX B: PERTURBED GALAXIES

Figures B1 and B2 shows examples of initial visual inspections of the 100 most massive galaxies extracted from the NewHorizon

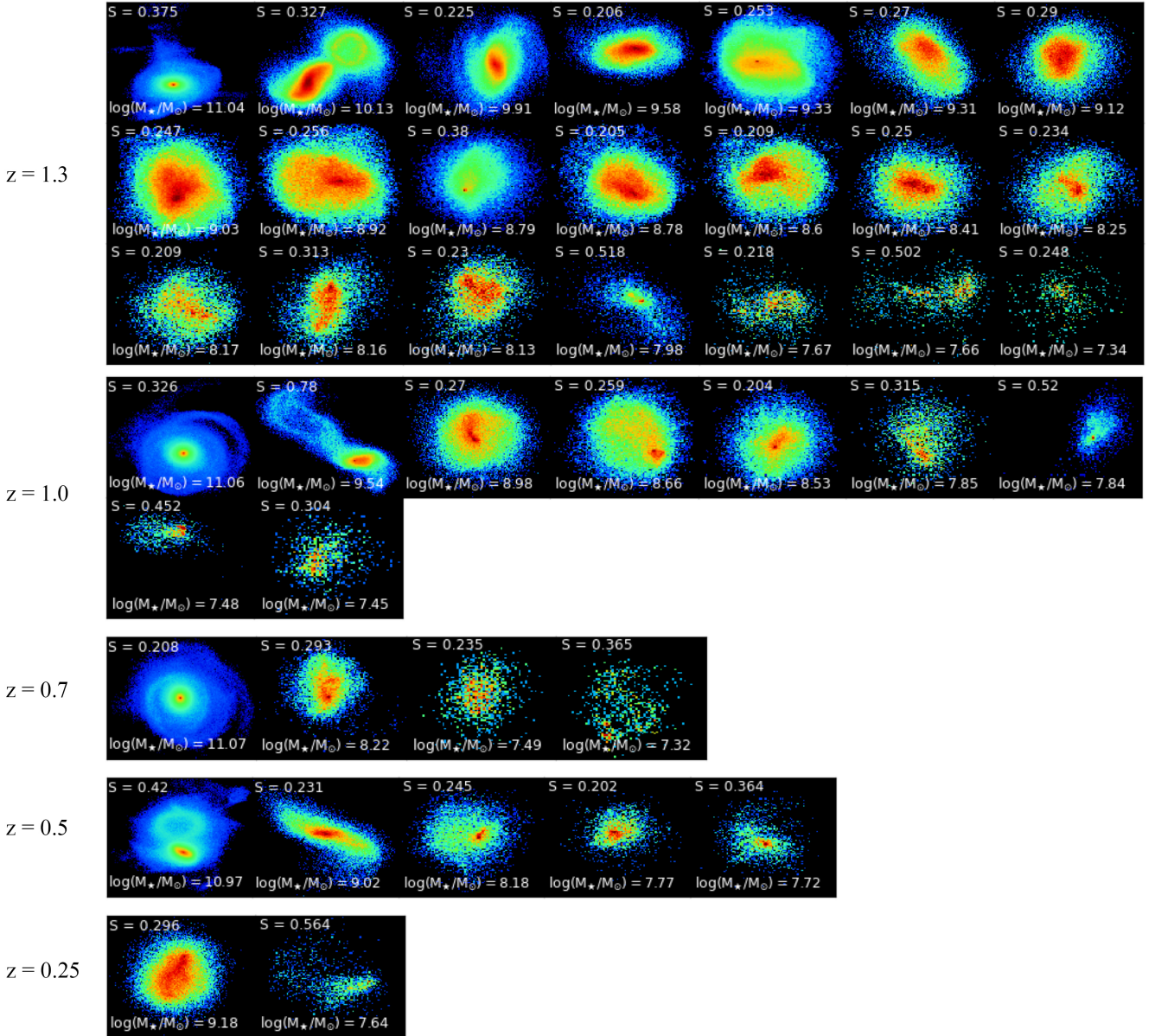


**Figure A1.** In this figure, we present, for the readers interest and discussion, the stellar surface density face-on projections of all the galaxies that we confirm as barred at each redshift. The strength of their bar is indicated in the top left corner, while their stellar mass is given at the bottom left. These barred galaxies are confirmed as such by requiring a bar detection in both detection methods applied. It is clear that there are no clear, large, elongated bars in this simulation and that the bars detected here are mostly small and/or rather perturbed. Confirmation of a bar is based solely on agreements between the methods and that our 'barred' galaxies refers to these theoretical or putative bars. All bars are short-lived (only detected at their given redshift) with one exception - that of the galaxy presented in Figure 1, which remains strongly barred from  $z = 1.3$  - 0.7 and can be presented as the first galaxy at each  $z = 1.3$ , 1.0 and 0.7 in this Figure.

Simulation at  $z = 1.3$  and at  $z = 0.25$  (with masses ranging from  $\sim 10^9 M_\odot$  to  $\sim 10^{11} M_\odot$ ). These grids were used to perform visual inspections on all the galaxies in the samples at each redshift in order to determine the number of galaxies that may potentially be barred. However, almost none of these were clear, strong, elongated bars. It is also apparent that these galaxies are highly perturbed, even at  $z = 0.25$ , making any visual detection of smaller, more perturbed bars challenging. These grids are presented here to highlight the complications involved in attempting to detect bars visually (especially at high redshift) due to the largely perturbed nature of these galaxies.

### APPENDIX C: BAR PROPERTIES IN THE VELOCITY BASED METHOD

Figure C1 presents plots of both bar strength and bar length vs stellar mass as calculated by the velocity method for comparison with the corresponding plot from the surface density method (Figure 4). From this, we find the same trends between the two methods, that being that we find a slight anti-correlation between bar strengths and galaxy mass at  $z = 0.25$  only and no correlation for bar lengths. We also find that there is almost no evolution in this relation between the bar strength and galaxy mass with redshift and that the higher mass

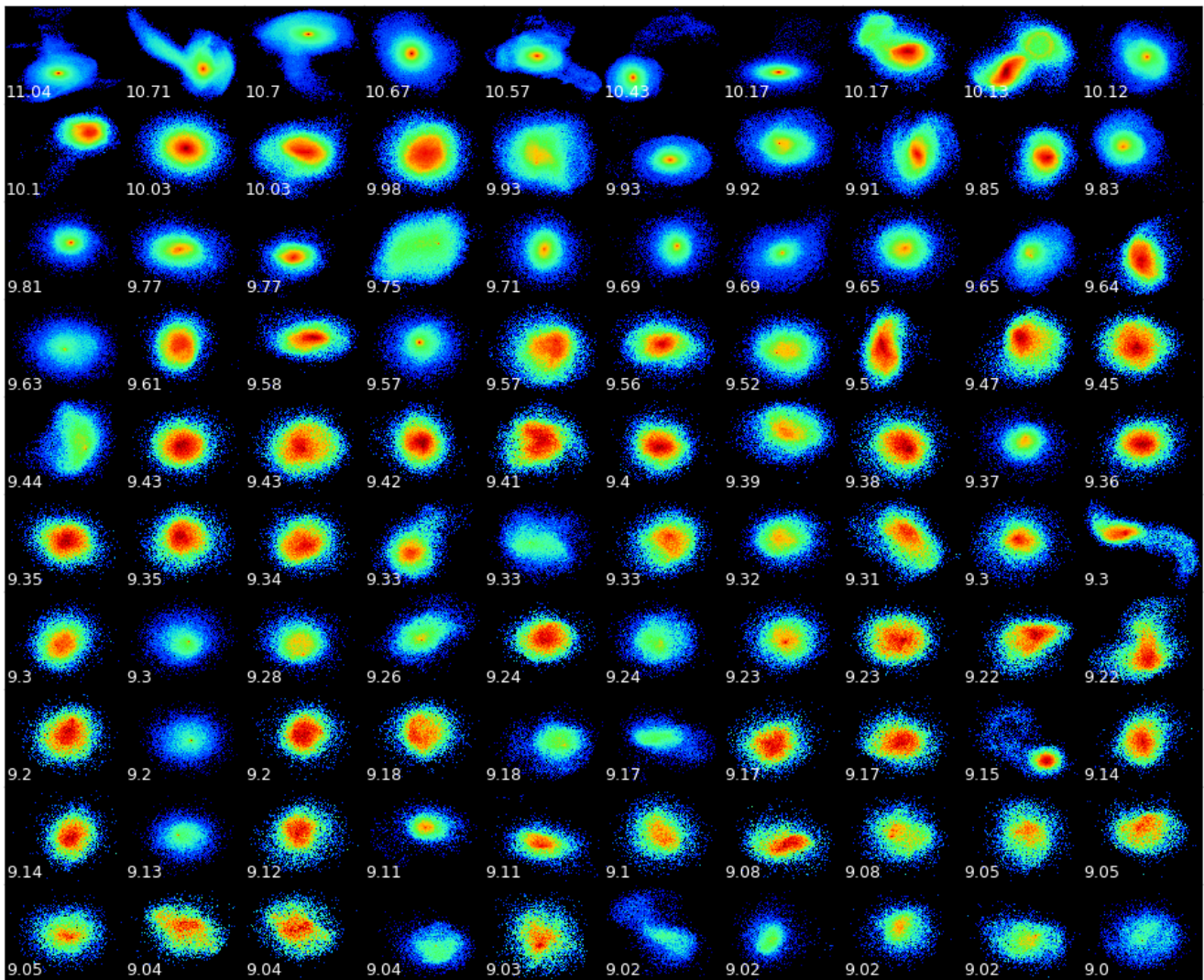


**Figure B1.** Initial visual inspection of the 100 most massive galaxies extracted from NEWHORIZON at  $z = 1.3$  (the logarithm of the stellar mass of each galaxy is represented by the number on the given panel i.e. the top left galaxy has a stellar mass  $M_{\star} = 10^{11.04} M_{\odot}$ ). It is clear that these galaxies are highly turbulent and that there are no clear, strong, elongated bars in any of the galaxies that could be seen visually at any of the redshifts. The surface density maps are plotted for  $50 \times 50 \text{ kpc}^2$  and the colour coding scale is logarithmic as in Figures 1 and 2.

galaxies tend to hold longer bars. By comparing between the two methods, we confirm a potentially barred galaxy as such. However, this does highlight biases in each method whereby these methods produce false positives and can incorrectly identify a galaxy as barred when used on their own. As discussed in the text, this could lead to current or future bar studies being biased to certain bar-like features without the incorporation of a secondary detection method.

#### APPENDIX D: LINEAR STABILITY OF TOY MODEL WITH VARYING BUDGE & HALO MASS

In this appendix we briefly revisit the seminal toy model of Aoki et al. (1979) to compute quasi-analytically the fastest growing modes of a Toomre-Kuzmin disc, as a proxy for the onset of bar formation. For the purpose of this paper, we extend it by accounting for the relative mass fraction in a passive halo and bulge, while keeping

the total disc-plus-bulge mass constant, allowing for mass transfer from the disc to the bulge on the one hand, and from the cosmic web to the galactic disc on the other hand. This provides us with a qualitative proxy for the trend found in the main text, i.e. that both reduced disc mass and bulge growth quench bar formation. We rely on two significant (simplicity driven) caveats: i) the disc is assumed to be razor thin, gaseous, isolated; ii) we limit our analysis to the computation of the linear growth rates of *global* bi-symmetric perturbations (i.e. beyond a local radial criterion such as Toomre's  $Q$  number Toomre 1963).

While the model for describing the response of the individual entities is crude, the joint analysis of the ensemble of timelines reflecting diverse environments should provide us with a more accurate global picture. The derived growth rates are an alternative diagnostic for the dynamical state of the galaxies in the simulation. The assumption here is that their secular evolution with cosmic time can be approximated as a sequence of parameters in this model, so

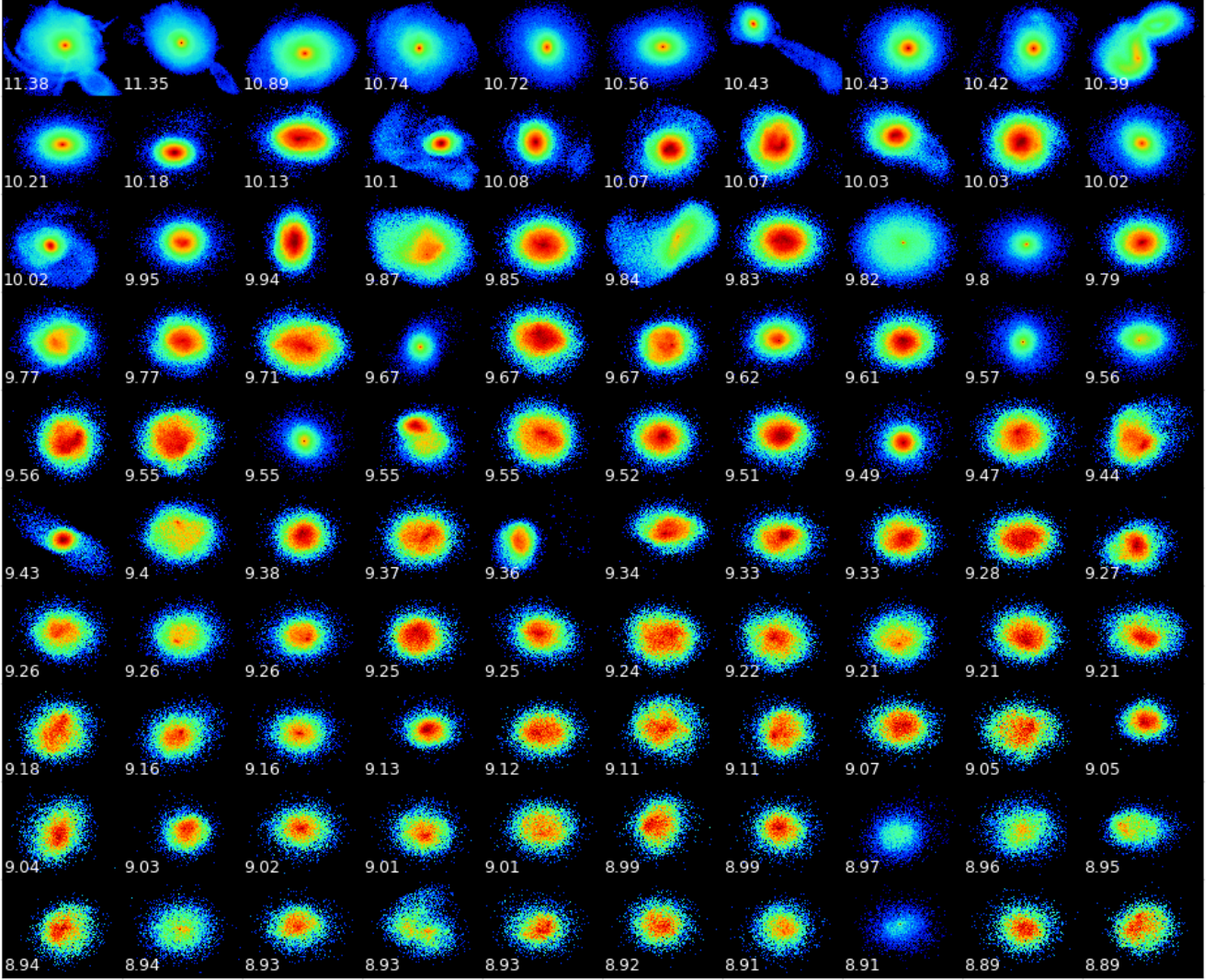


**Figure B2.** Initial visual inspection of the 100 most massive galaxies extracted from NEWHORIZON at  $z = 0.25$  (the logarithm of the stellar mass of each galaxy is represented by the number on the given panel i.e. the top left galaxy has a stellar mass  $M_{\star} = 10^{11.38} M_{\odot}$ ). One can still see that these galaxies are still highly turbulent highlighting the difficulty in identifying barred structure visually. The surface density maps are plotted for  $50 \times 50 \text{ kpc}^2$  and the colour coding scale is logarithmic as in Figures 1 and 2.

that, as the relative mass fractions and scale lengths change, the likelihood of a bi-symmetric instability developing into a strong bar varies.

### D1 Toy model setup

Consider a self-gravitating thin disc with a central spherical bulge and a spherical dark halo, with surface density  $\Sigma$ , and gravitational potential  $\Phi$ . For simplicity we will model this disc as though it was made of gas. Let  $\mathbf{v}$  be its velocity field and  $P$  its pressure. Then it obeys the hydro-dynamical and mean field equations

$$\frac{\partial \Sigma}{\partial t} + \nabla \cdot (\Sigma \mathbf{v}) = 0, \quad (\text{D1a})$$

$$\frac{\partial \mathbf{v}}{\partial t} + (\mathbf{v} \cdot \nabla) \mathbf{v} = -\frac{1}{\Sigma} \nabla P - \nabla \Phi, \quad (\text{D1b})$$

$$\Delta \Phi_{\text{disc}} = 4\pi G \Sigma \delta_{\text{D}}(z), \quad (\text{D1c})$$

where the total potential obeys  $\Phi = \Phi_{\text{bulge}} + \Phi_{\text{halo}} + \Phi_{\text{disc}}$ . Let us assume the gas is a polytrope with index  $\Gamma = 4/3$ , and fix the baryonic mass of the disc plus bulge to be  $M = M_{\text{disc}} + M_{\text{bulge}}$ . Then the system is described by the two parameters  $p = M_{\text{bulge}} / (M_{\text{disc}} + M_{\text{bulge}})$ , the bulge fraction, and  $q = M_{\text{disc}} / (M_{\text{disc}} + M_{\text{halo}})$ , the disc fraction.

The equilibrium state is modelled for simplicity by Plummer spheres (for the bulge and halo) and a Kuzmin-Toomre disc as

$$\Phi_{\text{disc}} = -\frac{GM(1-p)}{a_{\text{d}}} \left( \frac{1-\xi}{2} \right)^{1/2}, \quad (\text{D2})$$

and

$$\Phi_{\text{bulge}+\Phi_{\text{halo}}} = -\frac{GM}{a_{\text{d}}} \left[ \frac{a_{\text{d}}}{a_{\text{b}}} \frac{p}{\sqrt{1+(r/a_{\text{b}})^2}} + \frac{a_{\text{d}}}{a_{\text{h}}} \left( \frac{1}{q} - 1 \right) \frac{1-p}{\sqrt{1+(r/a_{\text{h}})^2}} \right],$$

where  $a_{\text{d}}$  is the scale length of the disc,  $a_{\text{h}}$  is the scale length of the halo,  $a_{\text{b}}$  that of the bulge, and where we introduced the reduced

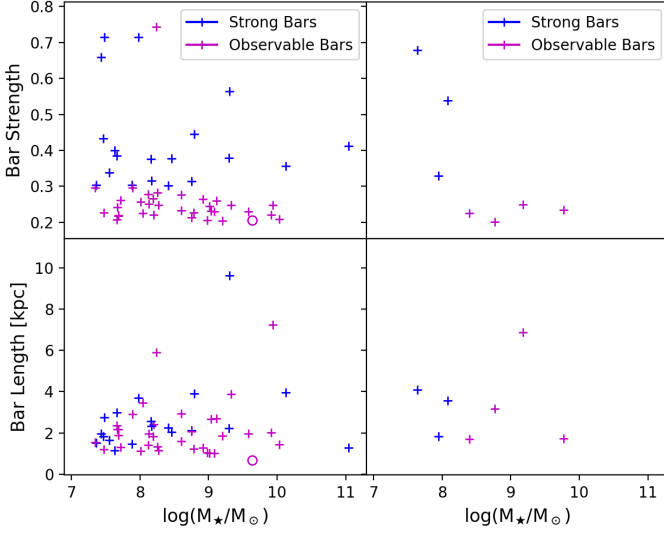


**Figure C1.** Figure showing bar strengths vs stellar mass (top panels) and bar lengths vs stellar mass (bottom panels) for  $z = 1.3$  (left panels) and  $z = 0.25$  (right panels). Bar strengths of both observable and strong bars are plotted for bars found in disc-dominated galaxies by the Velocity Harmonic Decomposition method. Bars of lengths greater than 1 kpc are marked with a cross and ‘short bars’ (those with lengths between 0.5 and 1.0 kpc) are marked as open circles. One can see that the most strongly barred galaxies tend to be those of the lowest masses whereas the higher mass galaxies tend to host weaker bars - similar to the surface density method (Figure 4).

radius,  $\xi = (r^2 - a_d^2)/(r^2 + a_d^2)$ . Then the angular velocity,  $\Omega$ , and the epicyclic frequency,  $\kappa$ , of the whole system read

$$\Omega(\xi) = \sqrt{\frac{GM(1-p)}{a_d^3}} \left[ \left( \frac{a_d}{a_b} \right)^3 \frac{p}{1-p} \left( \frac{1}{1+(r/a_b)^2} \right)^{3/2} \right. \quad (D3)$$

$$\left. + \left( \frac{a_d}{a_h} \right)^3 \left( \frac{1}{q} - 1 \right) \left( \frac{1}{1+(r/a_h)^2} \right)^{3/2} + \left( \frac{1-\xi}{2} \right)^{3/2} \left( 1 - \frac{\varepsilon_0}{(1-p)^{2/3}} \right) \right]^{1/2},$$

$$\frac{\kappa^2(\xi)}{2\Omega(\xi)} = 2\Omega(\xi) \left[ 1 + \frac{(1+\xi)(1-\xi)}{2\Omega} \frac{d\Omega}{d\xi} \right], \quad (D4)$$

where we introduced  $\varepsilon_0 = 0.1$  as the ratio of the internal and total energy which accounts for the strength of the pressure forces in the disc (given our choice of  $\Gamma$  polytropic index, see Aoki et al. 1979).

Let us linearise the system (D1a)-(D1b) in polar coordinates  $(r, \theta)$ , assuming an angular- and time-dependant scaling in  $\exp(im\theta - i\omega t)$ , and expand the first order perturbation of the two components of Euler’s equation and Poisson’s equation over normalized Legendre polynomial in  $\xi$  as, e.g.

$$\Sigma^1(r, \theta, t) = \frac{M(1-p)}{2\pi a_d^2} \left( \frac{1-\xi}{2} \right)^{3/2} \sum_{n=|m|}^{\infty} a_n^m P_n^{|m|}(\xi) e^{im\theta - i\omega t},$$

and a similar expression for the radial and the azimuthal component of the perturbed velocity field involving  $b_n^m$  and  $c_n^m$  coefficients. By design, this expansion satisfies Poisson’s equation. Following closely Aoki et al. (1979), upon injecting these expansions in the linearised system, multiplication by  $P_l^{|m|}(\xi)$  and integration over  $\xi$ , using the orthogonality relation (for all  $m$ )

$$\int_{-1}^1 d\xi P_n^{|m|}(\xi) P_l^{|m|}(\xi) = \delta_{nl}, \quad (D5)$$

we obtain the following eigen-problem for the growth rate  $\omega$  and the shape of the mode  $a_n^m$ :

$$\sum_{n=|m|}^{\infty} A_{ln} a_n^m + \sum_{n=|m|}^{\infty} B_{ln} b_n^m + \sum_{n=|m|}^{\infty} C_{ln} c_n^m = \lambda a_l^m, \quad (D6a)$$

$$\sum_{n=|m|}^{\infty} D_{ln} a_n^m + \sum_{n=|m|}^{\infty} A_{ln} b_n^m + \sum_{n=|m|}^{\infty} F_{ln} c_n^m = \lambda b_l^m, \quad (D6b)$$

$$\sum_{n=|m|}^{\infty} G_{ln} a_n^m + \sum_{n=|m|}^{\infty} H_{ln} b_n^m + \sum_{n=|m|}^{\infty} A_{ln} c_n^m = \lambda c_l^m, \quad (D6c)$$

where  $\lambda = \text{sign}(m) \omega / \sqrt{GM/a^3}$  and with the matrix elements,

$$A_{ln} = |m| \sqrt{\frac{a_d^3}{GM}} \int_{-1}^1 d\xi P_l^{|m|}(\xi) \Omega(\xi) P_n^{|m|}(\xi),$$

$$B_{ln} = 4\sqrt{1-p} \int_{-1}^1 d\xi P_l^{|m|}(\xi) \left( \frac{1-\xi}{2} \right)^{1/2} \frac{d}{d\xi} \left[ \left( \frac{1-\xi}{2} \right)^{5/4} P_n^{|m|}(\xi) \right],$$

$$C_{ln} = |m| \sqrt{1-p} \int_{-1}^1 d\xi P_l^{|m|}(\xi) \left( \frac{1-\xi}{2} \right)^{3/4} \left( \frac{1+\xi}{2} \right)^{-1} P_n^{|m|}(\xi),$$

$$D_{ln} = 4\sqrt{1-p} \left( \frac{1}{2n+1} - \frac{\varepsilon_0}{3(1-x)^{2/3}} \right) \times \int_{-1}^1 d\xi P_l^{|m|}(\xi) \left( \frac{1-\xi}{2} \right)^{5/4} \left( \frac{1+\xi}{2} \right) \frac{d}{d\xi} \left[ \left( \frac{1-\xi}{2} \right)^{1/2} P_n^{|m|}(\xi) \right],$$

$$G_{ln} = -|m| \sqrt{1-p} \left( \frac{1}{2n+1} - \frac{\varepsilon_0}{3(1-x)^{2/3}} \right) \int_{-1}^1 d\xi P_l^{|m|}(\xi) \left( \frac{1-\xi}{2} \right)^{3/4} P_n^{|m|}(\xi),$$

$$H_{ln} = \sqrt{\frac{a_d^3}{GM}} \int_{-1}^1 d\xi P_l^{|m|}(\xi) \frac{\kappa^2(\xi)}{2\Omega(\xi)} P_n^{|m|}(\xi),$$

and  $F_{ln} = 2/|m|A_{ln}$ . The integrals involving  $\Omega$  and  $\kappa$  are computed using a mid-point sampling rule, while the others are computed analytically by recursion.

Finding the growth rate of the mode,  $\omega$ , involves the computation of the eigenvalues of the infinite response matrix defined by Equations (D6a)-(D6c). In practice, we only have access to sequence of truncated matrices of varying size set by  $n_{\max}$ , from which we obtain lists of eigenvalues. Among those, we determine which are physically relevant, and which result from the truncation process. The latter either diverge to infinity or oscillate, which allows us to disregard them in favour of the subset which converges with  $n_{\max}$  (here typically  $n_{\max} \leq 170$ ). For each  $p, q$  we then select that with highest imaginary part,  $\omega_I = \text{Im}(\omega)$ , and build the corresponding map, within which we can assign some threshold below which we consider the  $m$ -fold symmetric mode grows too slowly for bar formation. In practice, the fastest growing mode shape and pattern speed displays sets of discontinuities as one increases  $p$  (or decreases  $q$ ), as eigenvalues corresponding to distinct physical branches become dominant. This can be seen as wiggles in the bottom left part of the light contours on figure 7.

Eventually, it could be of interest and more realistic to implement the fitting strategy presented in Ueda et al. (1985) to our sets of galaxies, while accounting for the detailed shape of the rotation curves (bulge included) and surface densities, in order to quantify statistically the dynamical stability of NewHorizon discs. Another

possible improvement would involve implementing a proper stellar stability analysis, following e.g. [Pichon & Cannon \(1997\)](#), which provides the flexibility in matching the distribution function and potential to that of the simulated galaxies. One could eventually account for the disc’s thickness, the live halo, or use the shape of the eigenvectors to match the pitch angle of the spiral response.

## D2 Mapping NEWHORIZON galaxies onto the $(p, q)$ plane

To interpret the NEWHORIZON galaxies in the context of Figure 7, we require a mapping of the galaxies onto  $(p, q)$  space. In the following mapping, we consider galaxies in the  $z = 1.3$  snapshot, but the mappings are similar for other snapshots. We measure the best mapping as follows. First, we fit the rotation curve of the dark matter halo,  $v_{c,\text{halo}}$  using the rotation curve of a Plummer sphere. We define the log likelihood function for the rotation curve evaluated at  $i$  radial points  $r_i$  in the galaxy midplane, with associated Poisson-like uncertainty  $\sigma_i$ , given the free parameters for the Plummer sphere representing the halo ( $a_h$ , the scale length of the halo, and  $M_{\text{halo}}$ , the mass of halo) as

$$\ln \mathcal{L}(v_c | a_h, M_{\text{halo}}) = -\frac{1}{2} \sum_i \left[ \frac{(v_{c,i} - v_{c,m}(r_i))^2}{\sigma_i^2} \right], \quad (\text{D7})$$

where the model rotation curve at each radial point  $r_i$  is given by

$$v_{c,m}(r_i) = \sqrt{2GM_{\text{halo}}r_i^2(a_h^2 + r_i^2)^{-(3/2)}}. \quad (\text{D8})$$

The uncertainty at each point on the rotation curve ( $\sigma_i$ ) is attributable to several factors, such as enclosed particle number, centre choice, and angular momentum rectification. Of these, the enclosed particle number contributes the most to the uncertainty budget. We therefore estimate the uncertainty on each point in the rotation curve using the reciprocal of the enclosed particle number at each radius, defining the minimum uncertainty to be 3%. In practice, the fits exhibit little dependence on the choice of uncertainty, such that a fixed uncertainty returns nearly the same parameter estimates. We then use EMCEE ([Foreman-Mackey et al. 2013](#)) to perform a Markov Chain Monte Carlo estimation of  $a_h$  and  $M_{\text{halo}}$ . Comparing the  $M_{\text{halo}}$  estimates to the true measured halo masses, we find a consistent bias to lower halo masses across the galaxy mass range related to the mismatch of the rotation curve profiles. The bias is constant with halo mass, and fixed at  $\log(M_{\text{halo,fit}}) - \log(M_{\text{halo,true}}) = -0.3$ . We correct for the bias below when estimating  $q$ . In addition to the bias, we also find modest variance ( $\pm 0.1$  dex) in the fit values, which contributes to uncertainty in the calculation of  $q$ .

Second, we fit a Toomre-Kuzmin rotation curve profile to the stellar disc component of the galaxies. Conveniently, the Plummer sphere and Toomre-Kuzmin disc have the same rotation curve profile in the  $z = 0$  plane, where we are performing the fits. Therefore, in equations D7 and D8, we need only change the subscripts to reflect that we are now estimating the disc parameters  $a_d$  and  $M_{\text{disc}}$ . We again use the same uncertainty estimation scheme, and estimate the parameters using EMCEE. We then compute the residuals for each disc galaxy. We define a galaxy as well-described by a single Toomre-Kuzmin disc component if the maximum relative error  $(v_{c,i} - v_{c,m}(r_i))/v_{c,m}(r_i) < 0.1$ . We find that  $> 90\%$  of galaxies (291 of 299 galaxies at  $z = 1.3$ ) meet this criteria.

We again compare the fit masses with the measured masses, finding similar bias and variance as in the halo (i.e. with no dependence on galaxy mass). We correct for the bias below when computing  $q$ . We may also compare the fit  $a_d$  to the measured  $r_{v_{\star,\text{max}}}$  in Section 5.2, finding that  $\langle a_d/r_{v_{\star,\text{max}}} \rangle = 0.6$ . For the galaxies

that are well-fit by a Toomre-Kuzmin disc and Plummer halo, we define  $\log q = \log(M_{\text{disc}}/(M_{\text{halo}} + M_{\text{disc}}))$  and  $p = 0$ . We find, after correcting for the bias in halo mass, that the galaxies are well-fit by the relation  $\log q_{z=1.3} = 0.6 \log(M_{\text{halo,true}}) - 7.5$ , resulting in  $\langle \log q \rangle = -1.7^{+0.3}_{-0.4}$  for a ‘typical’ galaxy in the sample at  $\log(M_{\text{halo}}) = 9.7$ . We therefore define  $(p, \log q) = (0.0, -1.7)$  as the location in  $(p, \log q)$  space for a typical bulgeless galaxy. From the fits to the galaxies, we find that  $\langle a_h/a_d \rangle = 2.8 \pm 0.3$ , which we use to inform the toy model construction. This ratio is valid for all galaxies, whether or not they are bulge-hosting.

Through visual inspection, we define galaxies which have maximum relative error  $> 0.1$  as ‘bulge-hosting’ galaxies, which require a second component. The galaxies that require a second component are those at the high mass end, as expected from the rotation curve decomposition in Section 5.2 and Figure 6. These galaxies also have larger  $\log q$  values on average, following the trend line listed above, such that if  $p = 0$ , they may fall in the instability regime. We estimate the bulge component for these galaxies using a two-component model for the rotation curve,

$$v_{c,m}(r_i) = \left[ 2Gr_i^2 \left( \frac{M_{\text{disc}}}{(a_d^2 + r_i^2)^{3/2}} + \frac{M_{\text{bulge}}}{(a_b^2 + r_i^2)^{3/2}} \right) \right]^{1/2}, \quad (\text{D9})$$

where we require that  $a_b < a_d$  and  $M_{\text{bulge}} < M_{\text{disc}}$ . These criteria enforce the disc as the dominant mass component, and require that the bulge be compact relative to the disc, consistent with what is observed in the galaxies by visual inspection. The rest of the likelihood function is unchanged apart from the addition of the dependence of the data on two extra parameters. From the fits to these galaxies, we find that  $\langle a_d/a_b \rangle = 20 \pm 4$ , which we use to inform the toy model construction. In practice, we then end up with ‘maximal’ disc components (i.e. contributions from the Toomre-Kuzmin disc that match the rotation curve when  $r$  is large). Also from the fits, we compute the  $p$  values to be  $p \approx 0.2$ . We therefore define  $(p, \log q) = (0.2, -1.0)$  as the location in  $(p, \log q)$  space for a typical bulge-hosting galaxy.

We also perform a cursory inspection of galaxies at  $z = 0.25$ , the lowest redshift analysed in our sample. The parameters of the toy model remain largely unchanged, with a modest increase in  $a_d/a_b$  (i.e. bulges have become more concentrated), which has the effect of moving the stability line towards increasing  $x$ . We find that on average,  $\log q_{z=0.25} = \log q_{z=1.3} + 0.2$ . A significant fraction of the disc galaxies still do not appear to host a bulge, while the typical bulge-hosting galaxy has increased the location in  $p$ -space to 0.25. Taken together, the disc-dominated galaxies appear to be growing self-similarly while the bulges grow at a modestly faster rate and with decreasing scale length, which serves to keep the discs stable against bar formation.

## APPENDIX E: HIGH MASS BAR FRACTIONS

In this section, we present the results of our analysis in terms of bar fractions when placing a stellar mass cut of  $M_{\star} \geq 10^{10} M_{\odot}$  so as to provide a more versatile comparison to observations in the literature.

**Table E1.** The results of our analysis in terms of spiral fractions and bar fractions for 'strong bars' ( $S \geq 0.3$ ) and 'observable bars' ( $S \geq 0.2$ ) at redshifts  $z = 1.3, 1.0, 0.7, 0.5$  and  $0.25$ . The bar fractions as obtained by both bar detection methods described in Section 3 are shown. The confidence intervals presented have been estimated using the (Bayesian) beta distribution quantile technique (Cameron 2011). We also present numerical values in the parenthesis. We have applied a mass cut  $M_{\star} \geq 10^{10}M_{\odot}$  so as to compare more directly to previous observational studies. See Figure 1 for our full results.

Redshift	Spiral Fraction (Number of Spirals)	Method	Bar Fractions (Number of Bars)	
			Strong Bars	Observable Bars
1.3	0.923 <sup>+0.026</sup> <sub>-0.140</sub> (12)	Surface Density	0.167 <sup>+0.155</sup> <sub>-0.059</sub> (2)	0.250 <sup>+0.156</sup> <sub>-0.083</sub> (3)
		Velocity	0.167 <sup>+0.155</sup> <sub>-0.059</sub> (2)	0.250 <sup>+0.156</sup> <sub>-0.083</sub> (3)
1.0	1.000 <sup>+0.010</sup> <sub>-0.103</sub> (16)	Surface Density	0.063 <sup>+0.119</sup> <sub>-0.020</sub> (1)	0.063 <sup>+0.119</sup> <sub>-0.020</sub> (1)
		Velocity	0.063 <sup>+0.119</sup> <sub>-0.020</sub> (1)	0.063 <sup>+0.119</sup> <sub>-0.020</sub> (1)
0.7	0.857 <sup>+0.050</sup> <sub>-0.140</sub> (12)	Surface Density	0.0 (0)	0.083 <sup>+0.149</sup> <sub>-0.028</sub> (1)
		Velocity	0.0 (0)	0.083 <sup>+0.149</sup> <sub>-0.028</sub> (1)
0.5	0.765 <sup>+0.072</sup> <sub>-0.128</sub> (13)	Surface Density	0.077 <sup>+0.140</sup> <sub>-0.026</sub> (1)	0.077 <sup>+0.140</sup> <sub>-0.026</sub> (1)
		Velocity	0.077 <sup>+0.140</sup> <sub>-0.026</sub> (1)	0.154 <sup>+0.147</sup> <sub>-0.054</sub> (2)
0.25	0.714 <sup>+0.077</sup> <sub>-0.114</sub> (15)	Surface Density	0.0 (0)	0.0 (0)
		Velocity	0.0 (0)	0.0 (0)

**Table E2.** The final results of our bar search analysis in terms of bar fractions calibrated between the two methods whereby a barred galaxy is confirmed as such if said galaxy found to be barred in by both methods. The bar fractions (and number of barred galaxies) are shown for redshifts  $z = 1.3, 1.0, 0.7, 0.5$  and  $0.25$ . The confidence intervals presented have been estimated using the (Bayesian) beta distribution quantile technique (Cameron 2011). We have applied a mass cut  $M_{\star} \geq 10^{10}M_{\odot}$  so as to compare more directly to previous observational studies. See Figure 2 for our full results.

Redshift	Final Bar Fractions (Number of Bars)	
	Strong Bars	Observable Bars
1.3	0.167 <sup>+0.155</sup> <sub>-0.059</sub> (2)	0.167 <sup>+0.155</sup> <sub>-0.059</sub> (2)
1.0	0.0 (0)	0.063 <sup>+0.119</sup> <sub>-0.020</sub> (1)
0.7	0.0 (0)	0.083 <sup>+0.149</sup> <sub>-0.028</sub> (1)
0.5	0.077 <sup>+0.140</sup> <sub>-0.026</sub> (1)	0.077 <sup>+0.140</sup> <sub>-0.026</sub> (1)
0.25	0.0 (0)	0.0 (0)